

Date of publication xxxx 00, 0000, date of current version xxxx 00, 0000.

Digital Object Identifier 10.1109/ACCESS.2024.Doi Number

High Gain Narrow Beam MIMO Array Antenna operating at n260 Band for Millimeter Wave Applications

Parveez Shariff B. G.¹, (Graduate Member, IEEE), Tanweer Ali¹, (Senior Member, IEEE), Pallavi R. Mane¹, (Senior Member, IEEE), Sameena Pathan², Saad Hassan Kaini³, Bal S. Virdee⁴, (Senior Member, IEEE), and Hala Mostafa, (Member, IEEE)

¹Department of Electronics and Communication Engineering, Manipal Institute of Technology, Manipal Academy of Higher Education, Manipal 576104, India

²Department of Information and Communication Technology, Manipal Institute of Technology, Manipal Academy of Higher Education, Manipal 576104, India

³Centre for Telecommunication Research & Innovation (CETRI), Universiti Teknikal Malaysia Melaka, Melaka 76100, Malaysia

⁴Center for Communications Technology, London Metropolitan University, London N7 8DB, United Kingdom

⁵Department of Information Technology, College of Computer and Information Sciences, Princes Nourah bint Abdulrahman University, Riyadh 11671, Saudi Arabia

Corresponding author: Tanweer Ali and Sameena Pathan (e-mail: tanweer.ali@manipal.edu; sameena.bp@manipal.edu).

ABSTRACT This paper introduces a novel four-port antenna array designed for n260 band operation, specifically addressing challenges like path loss fading and multipath effects commonly encountered in millimeter-wave frequencies in urban settings. The proposed 4×4 MIMO antenna array operates in the n260 band, offering high gain and a narrow beam, with an extended design enabling spatial and pattern diversity to mitigate multipath effects effectively. The single-element antenna combines elliptical and circular rings fed by a quarter-wave transformer. Its fundamental frequency of 30 GHz is suppressed by integrating circular rings in the radiator and a slot in the ground plane, which enhances its first harmonic at 38.5 GHz while generating vertical polarization. The array antenna improves the fractional bandwidth (FB) to 8.4%, with a frequency range of 36.76-39.92 GHz, and achieves dual broadside beams at $\pm 37^\circ$ angles with a gain of 16.7 dBi. Additionally, it exhibits exceptionally low cross-polarization (-80 dB), minimizing cross-talk effects. The MIMO configuration demonstrates excellent isolation ($|S_{21}| > 26$ dB and 31.2 dB) while maintaining similar FB and radiation pattern characteristics as the array antenna. This robust design, incorporating both spatial and pattern diversity, makes it highly suitable for 5G wireless applications.

INDEX TERMS 5G, Array, MIMO antenna, millimeter wave

I. INTRODUCTION

Globally, 5G communication opens the broad horizon for various data-hunger applications operating with low latency. The spectrum for 5G specified by the International Telecommunication Union (ITU) is from 30-300 GHz. This spectrum offers tremendous bandwidth, however, the path loss also increases. To address this issue, high-gain array antennas are essential. The high gain array antenna could improve the signal-to-noise (SNR) ratio in a lossy environment. However, mmWave communication in urban and other terrestrial scenarios is quite challenging due to signal blockage by various surrounding objects [1]. This leads to a multipath effect, and most of the time, blockage sets up a non-line-of-sight (NLOS) communication, and the

signal level drops significantly [2]. This issue can be addressed by the multiple-input-multiple-output (MIMO) antenna. With the MIMO antenna, the multipath signals can be identified through angular and delay resolution, thus making the communication reliable [3]. However, the criticality in the MIMO antenna structure is the issue of mutual coupling [4], [5] where the radiated energy from one antenna is coupled to an adjacent or nearby antenna. The coupling degrades the MIMO antenna performance, however, with the techniques of parasitic elements [6], defecting ground plane [7], decoupling structures [8], electromagnetic bandgap structures [9], metamaterial-based

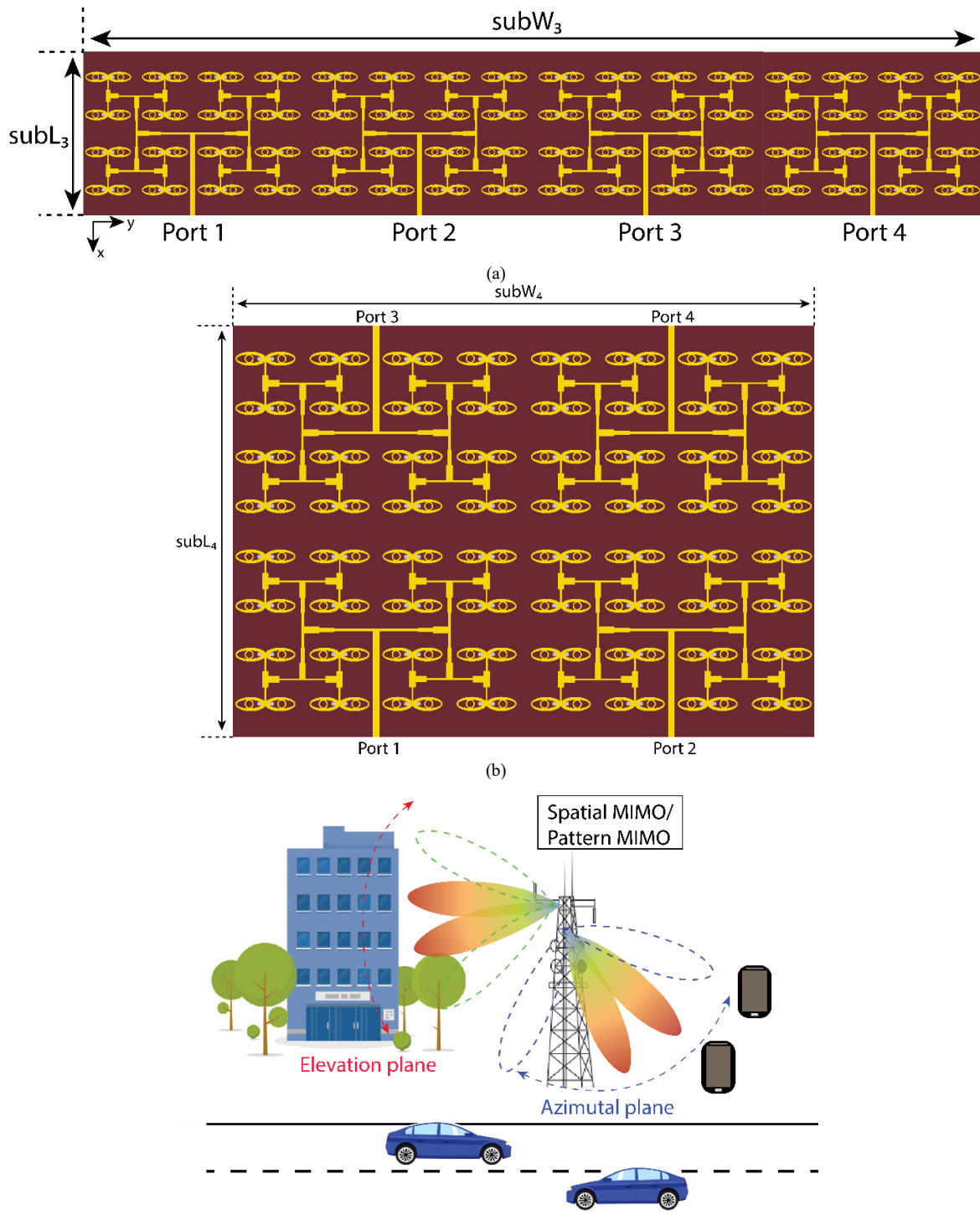


FIGURE 1. Proposed (a) spatially-oriented and (b) pattern-oriented MIMO antenna structures. The dimension in mm as follows: $subL_3 = 26$, $subW_3 = 143$, $subL_4 = 50$, and $subW_4 = 71$. (c) Illustrating the application scenario of the proposed MIMO antenna forming dual-beam, and with a beamforming network, it could steer the beam.

[10], and self-decoupling structures [11], the coupling can be suppressed. Therefore, the MIMO antenna with high gain could improve the SNR and address the multipath effect.

Some of the high gain antenna structures are reflectarray antennas [12], series-fed arrays [13], 3D printed lens-horn antenna [14], biconical antenna with metal lenses [15],

frequency-selective surfaces [16], waveguide antenna array [17], dielectric-resonators (DRA) with microstrip structures [18], [19], [20] and parallel-fed planar array antennas [21]. The reflect array, 3D printed lens, and waveguide array have achieved high gain in the order of 20 to 30 dBi; however, the design and fabrication of such structures are complex at

mmWave and above. It requires precise milling, which increases the cost. The biconical antenna [15] is also a complex structure that has achieved bidirectional radiation with a low gain of 8 dBi. The planar array antennas are mostly single-layer structures that adopt series or parallel feed mechanisms. Both methods have its own merits and limitations. On the other hand, the DRA with microstrip structures [18], [19], [20] improves the gain and other parameters, however, it also makes the fabrication complex and increases the antenna profile. The designs in [13] and [21] achieved broadside radiation with a decent gain of 16 dBi. However, the overall dimension of [21] is quite large.

Instead of a single broadside beam, a multi-beam antenna could provide better coverage for 5G communications. In [22], a MIMO antenna configuration is tilted relative to each other on a planar surface to achieve beams at different angles. Also, through slots in the ground plane, better isolation is demonstrated. The other method to steer the beam is to use the butler matrix, as discussed in [23]. Here, dielectric resonators with EBG structures are used; however, the gain achieved is still low at 7.85 dBi with wide half-power beamwidth (HPWB). In [24], a set of planar antenna structures are excited separately with an active device of 60 p-i-n diodes to steer the beam. Yet the gain of the antenna is low at 5 dBi, and with such a large number of active devices, the noise and non-linearity and the overall cost increase.

This article focuses on the design of a high gain and low-cost antenna operating in the n260 band, achieving robust |S-parameter| performance for both spatial and pattern diversity MIMO arrangements. The radiator of the single-element antenna embeds two elliptical and circular rings, which is fed by a 50 Ω feed line. For impedance matching between feed and antenna, a quarter-wave transform of 100 Ω is used. The combination of a circular ring and slot in the ground plane suppresses the fundamental frequency at 30 GHz and generates the resonance at first harmonic, that is, at 38.5 GHz. This antenna is arranged in a 4 × 4 array to further improve the gain and radiation pattern. Due to two different spacing along the x- and y-axis, the array antenna resulted in a dual-beam in a broadside direction at an elevation angle ($\theta = \pm 37^\circ$). The dimension of a 4 × 4 array is $3.34\lambda \times 4.5\lambda$ (at 38.5 GHz). Later, the array antenna is expanded to a four-port spatial and pattern diversity MIMO antenna for comparative analysis, its design structure is shown in Figs. 1(a) and 1(b).

The purpose of considering spatial and pattern MIMO structure is to study the surface wave coupling effect for different orientations; otherwise, they have similar performance characteristics in terms of reflection coefficient and radiation pattern. The spatial MIMO antenna has a measured bandwidth ranging from 36.2-40* GHz with minimum isolation |S21| of > 29 dB. On the other hand, the pattern MIMO antenna bandwidth ranges from 35.7-40* GHz (* indicating the limitation of measuring device only up to 40 GHz) with minimum isolation |S21| of > 31.2 dB. Both MIMO structures achieve a maximum gain of 16.7 dBi with a total

efficiency of 83.8%. Both the MIMO antenna structures offer some degree of beam steering. The linearly arranged spatial MIMO antenna with all four ports excited with zero phase shift, increases the gain to 23 dBi, constructively narrowing the beam to 4.5° at $\theta = \pm 37^\circ$. On the other side, the pattern MIMO antenna forms a narrow beam at both $\varphi = 0^\circ$ and $\theta = \pm 37^\circ$, which is 11° and 09° , respectively. With the beamforming network, the spatial MIMO antenna could steer the beam in the azimuthal/elevation plane based on the antenna orientation; however, with a pattern MIMO antenna, it could steer the beam in both elevation and azimuthal plane. Fig. 1(c) demonstrates the application scenario of the proposed MIMO antenna structures.

II. SINGLE-ELEMENT ANTENNA

A. Design

A conventional circular patch antenna at 38.5 GHz may have a radius of approximately 1.4 mm, generally resulting in a 2% fractional bandwidth (FB) with 7 dBi directivity. A similar result may appear for a rectangular patch antenna. However, with the partial ground and defecting patch technique, the FB could be improved to 5-7%, but this will reduce the directivity and gain in the broadside direction [25], [26]. Techniques such as capacitively coupled parasitic elements [27], [28] and substrate-integrated waveguide (SIW) feed [29] could improve directivity while maintaining the desired FB. Another technique to enhance FB and directivity is through the use of a complementary-split-ring-resonator (CSSR) [30] and meandered parasitic element [31]. However, these techniques and slots or slits in small patches in a process to enhance FB poses fabrication challenges while designing at higher frequencies.

Consequently, a novel antenna structure with a broader width (ER_w) and reduced length is proposed in this section. The area of the circular patch is distributed in a dual elliptical ring shape, thereby increasing the aperture area, through which the gain is improved. Rogers 5880 substrate is chosen to reduce the dielectric losses, having a loss tangent of 0.0009 and thickness of 0.254 mm. The antenna combines elliptical and circular rings fed by a 50 Ω feed line. A 100 Ω quarter-wave transform is used for impedance matching between the patch and feed line, thus achieving better directivity, resonance, and FB. The novel structure is illustrated in Fig. 2.

The base design is an elliptical structure with an elliptical slot etched inside it, whose fundamental resonance (f_{r0}) is derived from the elliptical cavity model Equation (1) [32] for TM_{10} mode.

$$f_{r0} = \frac{c}{2\pi\sqrt{\epsilon_{eff}}} \cdot \sqrt{\left(\frac{m}{EMX_1}\right)^2 + \left(\frac{n}{EMX_2}\right)^2} \quad (1)$$

where c is the velocity of light in free space (3×10^8 m/s), ϵ_{eff} is the effective permittivity calculated as $\frac{\epsilon_r + 1}{2}$, which is

1.6 for the relative permittivity (ϵ_r) of 2.2. The m and n are the traverse electric or magnetic fundamental modes, which, in our case $m = 1$ and $n = 0$.

The width (EMX_1) of the elliptical structure is significant in achieving impedance matching, whereas the height (EMX_2) is responsible for tuning antenna bandwidth. Since the desired mode is TM_{10} , the Equation (1) will be deduced to (2).

$$f_{r0} = \frac{c}{2\pi\sqrt{\epsilon_{eff}}} \cdot \sqrt{\left(\frac{m}{EMX_1}\right)^2} \quad (2)$$

Rearranging the Equation (2) and solving for the fundamental frequency of 30 GHz, the elliptical width (EMX_1) results in 3.95 mm. This leads to the generation of TM_{10} mode, however, with poor impedance matching. Further, an elliptical slot is added with a width and height of EMn_1 and EMn_2 . This has increased the electrical length such that the total circumference of the inner elliptical ring equals 0.66λ at 30 GHz, which is close to $\frac{3}{4}$ of the wavelength. Thus, a resonance at 30 GHz is observed, but with lower FB, as depicted in Fig. 3. On the other hand, the total width (ER_w) of the combined elliptical ring is equal to $\frac{3}{4}$ of wavelength (at 30 GHz). Thus, the current flow on the elliptical ring along the y-axis, and due to $\frac{3}{4}$ wavelength long structure, it give rise to horizontal polarization, as illustrated in Fig. 4.

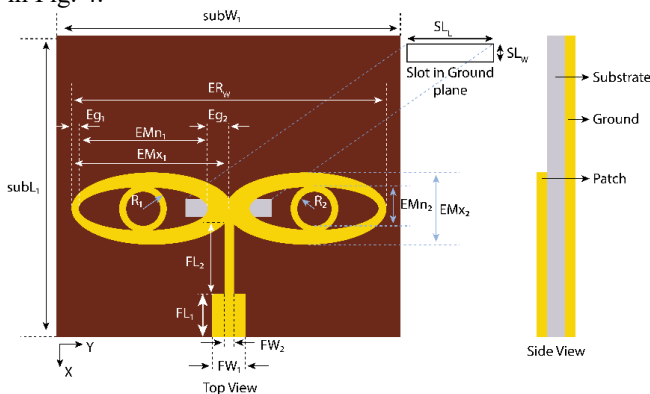


FIGURE 2. Single-element antenna design with top and side view. The dimensions in mm are as follows: $FW_1 = 0.78$, $FW_2 = 0.22$, $FL_1 = 1$, $FL_2 = 1.66$, $EMx_1 = 3.69$, $EMx_2 = 1.69$, $EMn_1 = 3$, $EMn_2 = 1$, $R_1 = 0.55$, $R_2 = 0.4$, $Eg_1 = 0.17$, $Eg_2 = 0.64$, $ER_w = 7.32$, $SL_l = 2$, $SL_w = 0.4$, $SubL_1 = 7$, $SubW_1 = 8$.

Further, to suppress the fundamental frequency and generate the first harmonic at 38.5 GHz, circular rings (consider R_2 radius) inside the elliptical rings are added. This has reduced the electrical length of the surface current to 0.46λ at 30 GHz. Also, this electrical length is equal to $\frac{3}{4}$ of wavelength at 46 GHz. Thus, the antenna generates its first harmonic at 46 GHz instead of 38.5 GHz. However, the objective of the antenna is to operate in the n260 band. Therefore, to drift the first harmonic to 38.5 GHz and to suppress the fundamental frequency, a slot in the ground plane is strategically placed below the radiator, as a result, resonance is achieved at 38.5 GHz, as demonstrated in Fig. 3. With this modification, the antenna resulted in TM_{10} with vertical

polarization, which is better comprehended from surface vector current in Fig. 4.

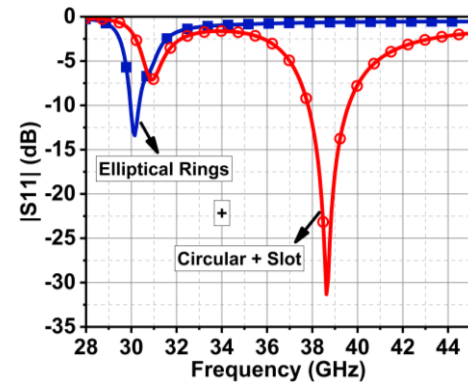


FIGURE 3. Reflection coefficient curve of an antenna with only elliptical rings and proposed antenna.

Fig. 4. Illustrates the surface current of the elliptical ring antenna at 30 GHz and 38.5 GHz. At 30 GHz, there is good impedance matching, and $> 90\%$ of the power from the port is fed to the antenna. Due to an elliptical structure and its orientation along the y-axis, the surface current flows along the horizontal axis, generating horizontal polarization. The current at the antenna lags by 90° relative to the port because of the use of a quarter-wave transformer. Consequently, the horizontal current oscillation is shown at 90° and 270° . At 90° and 270° phase, the current from both ellipses are in opposite directions along the y-axis, it is due to the electrical length of 0.66λ (at 30 GHz), which is close to $\frac{3}{4}$ of wavelength, generating TM_{02} mode. With the addition of circular rings, the electrical length is shortened, that is, 0.29λ at 30 GHz, which is close to a quarter-wavelength, and 0.45λ at 46 GHz, a half-wavelength. As a result, a resonance at 30 GHz and 46 GHz is observed, however, with poor impedance matching. Further, the antenna is tuned by etching the ground slot, whose width is a quarter-wavelength long that is 0.25λ at 38.5 GHz. Due to the slot, the current takes a longer path; thus, by increasing the slot width, the electrical length increases, and thereby, the resonance drifts to the lower frequency and vice versa. Now, the electrical length of the patch is 0.55λ , and the slot is 0.25λ (at 38.5 GHz). Similar to the cavity model of the slotted waveguide structure, the horizontal slot in the ground plane of our antenna perturbs the surface current, which in turn causes the electric field to align vertically, generating vertical polarization, as shown in Fig. 4. The arrows in black indicates the current in ground plane and red on patch.

B. Modeling of an Antenna with Transmission Line

Generally, the resonance of the patch antenna is modeled by representing a parallel RLC lumped circuit. However, at millimeter-wave frequency, the dimensions of the proposed planar antenna structure are comparable with the wavelength. As a result, the voltage and current due to

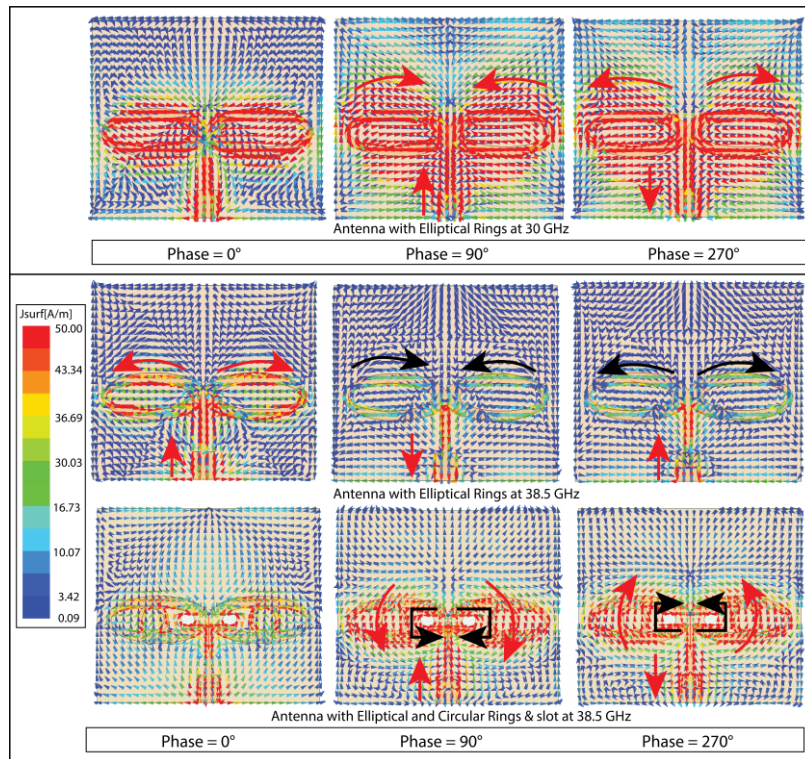


FIGURE 4. Surface current distribution of single-element antenna with and without circular rings and ground slots.

electromagnetic waves are different at various locations on the structure. Also, the structure will experience different phases at multiple locations. Thus, the entire antenna structure is divided into small units of circuit elements and modeled as a transmission line. The microstrip line is represented by inductance (L) with low resistance (R), and the slot in the structure or the gap between the transmission lines is indicated by shunt capacitance (C). The simplified transmission line model of the single-element antenna is shown in Fig. 5. The feed line Z_{F1} has a characteristic impedance of 50Ω and Z_{F2} is a quarter-wave transform having a characteristic impedance of 100Ω . For analytical purposes, the feed line impedances are assumed to have zero reactive components. The impedance (Z_{in2}) at the input of Z_{F2} applies the special condition because of the quarter wave transform line, that is,

$$Z_{in2} = \frac{(Z_{F2})^2}{Z_L} \quad (3)$$

Thus, the overall input impedance Z_{in1} is,

$$Z_{in1} = Z_{F1} \frac{Z_{in2} + jZ_{F1} \tan(\beta_1 l_1)}{Z_{F1} + jZ_{in2} \tan(\beta_1 l_1)} \quad (4)$$

where β_1 is the phase constant indicating the phase change along the transmission line given as $2\pi/\lambda_g$, and the l_1 is its physical length. The λ_g is a guided wavelength at 38.5 GHz.

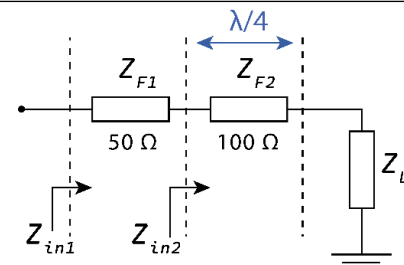


FIGURE 5. Generalized transmission line model of single-element antenna.

The geometry of the patch, along with the ground slot, is considered as a load Z_L , which is further split into a small transmission line model showcasing inductive and capacitive impedances. These are obtained by modeling the small transmission line as lumped components, for example, the impedance of Z_a is represented by a resistor R_a in series with an inductor L_a . Likewise, the entire Fig. 6 is modeled as small lumped components in the circuit simulator. Further, these values are tuned to match the results obtained from the electromagnetic solver. Later, from the lumped values, the impedances are computed. The inductive impedance of elliptical rings are Z_a and Z_b , whereas Z_{Ca} and Z_{Cb} are its shunt capacitive impedances. Likewise, the circular ring inductive and capacitive impedances are Z_{LP} and Z_{CP} . The slot in the ground plane is depicted by Z_{CG} , whereas the capacitance between the patch and ground plane is indicated by Z_{CC} , as shown in Fig. 6.

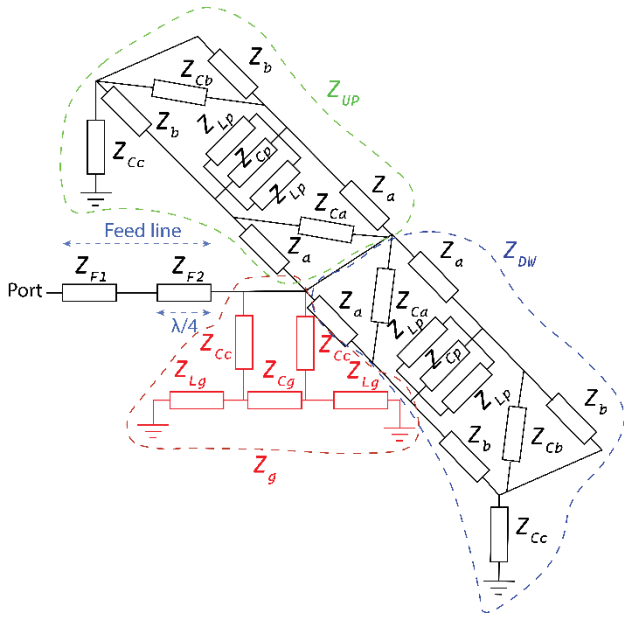


FIGURE 6. Representation of single-element antenna in transmission line model.

The load impedance Z_L is simplified in three steps by applying the delta-to-star and vice versa method, wherever applicable. The impedance Z_g , Z_{UP} and Z_{DW} , represents the impedance of the ground plane with slot, left patch geometry, and right patch geometry. The impedance of Z_g is find by solving equations (3) to (7),

$$Z_g = Z_1 + \left(\frac{Z_{Lg2} Z_{Lg3}}{Z_{Lg2} + Z_{Lg3}} \right) \quad (5)$$

where

$$Z_1 = \frac{(Z_{CC})^2}{2Z_{CC} + Z_{Cg}} \quad (6)$$

$$Z_3 = Z_2 = \frac{Z_{CC} Z_{Cg}}{2Z_{CC} + Z_{Cg}} \quad (7)$$

$$Z_{Lg2} = Z_{Lg} + Z_2 \quad (8)$$

$$Z_{Lg3} = Z_{Lg} + Z_3 \quad (9)$$

Further, the impedance of Z_{UP} and Z_{DW} is obtained using the Equations (8) to (21).

$$Z_{LPC} = \frac{(Z_{LP})^2 Z_{CP}}{(Z_{LP} Z_{CP})^2 + (Z_{LP})^2} \quad (10)$$

$$Z_{1b} = Z_{1a} = \frac{Z_{LPC} Z_a}{Z_{LPC} + Z_a + Z_{Ca}} \quad (11)$$

$$Z_{1c} = \frac{Z_{LPC} + Z_a + Z_{Ca}}{Z_{Ca} Z_a} \quad (12)$$

$$Z_{1ab} = Z_{1b} + Z_{1a} \quad (13)$$

$$Z_{2a} = \frac{(Z_{Cb})^2}{Z_b + Z_{1ab} + Z_{Cb}} \quad (14)$$

$$Z_{2b} = \frac{Z_b Z_{1ab}}{Z_b + Z_{1ab} + Z_{Cb}} \quad (15)$$

$$Z_{2c} = \frac{Z_{Cb} Z_{1ab}}{Z_b + Z_{1ab} + Z_{Cb}} \quad (16)$$

$$Z_{2ab} = Z_a + Z_{2b} \quad (17)$$

$$Z_{3a} = \frac{Z_{2c} Z_{2ab}}{Z_{2c} + Z_{2ab} + Z_{1c}} \quad (18)$$

$$Z_{3b} = \frac{Z_{2ab} Z_{1c}}{Z_{2ab} + Z_{1c} + Z_{2c}} \quad (19)$$

$$Z_{3c} = \frac{Z_{2c} Z_{1c}}{Z_{2c} + Z_{2ab} + Z_{1c}} \quad (20)$$

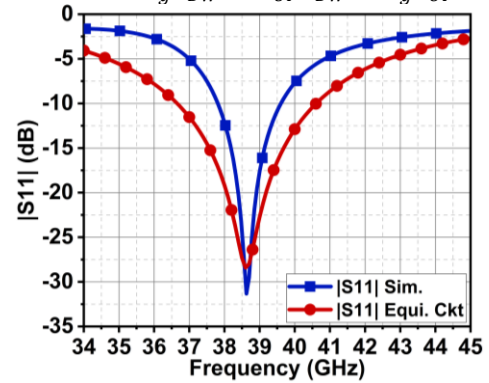
$$Z_{23a} = Z_{2a} + Z_{3a} \quad (21)$$

$$Z_{3bc} = Z_{3c} + Z_b \quad (22)$$

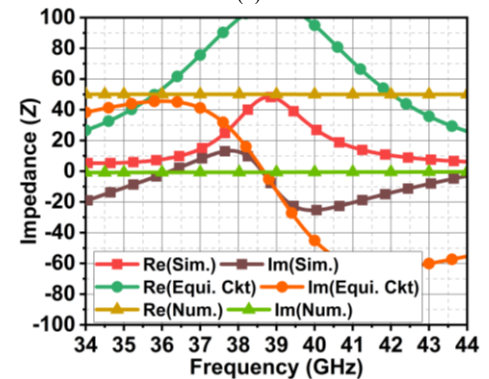
$$Z_{UP} = Z_{DW} = Z_{CC} + \frac{Z_{23a} Z_{3bc}}{Z_{23a} + Z_{3bc}} + Z_{3b} \quad (23)$$

The load impedance Z_L is given by,

$$Z_L = \frac{Z_{UP} Z_g Z_{DW}}{Z_g Z_{DW} + Z_{UP} Z_{DW} + Z_g Z_{UP}} \quad (24)$$



(a)



(b)

FIGURE 7. (a) Comparison of simulated and equivalent circuit reflection coefficient $|S_{11}|$ of single-element antenna. (b) Representing impedance obtained from simulation, circuit simulator, and numerical method.

The impedance values of Fig. 6 are estimated by modeling the single-element antenna using the AWR circuit simulator tool. Here, the impedances are tuned to match the simulated results of the antenna, and the comparison of these is presented in Fig. 7(a). The obtained final impedance values are: $Z_a = (15.12 + j21.77)\Omega$, $Z_b = (18.11 + j36.76)\Omega$, $Z_{Ca} = (-j6.66)\Omega$, $Z_{Cb} = (-j10.33)\Omega$, $Z_{LP} = (j10.15)\Omega$, $Z_{CP} = (-j27.55)\Omega$, $Z_{CC} = (-j25.4)\Omega$, $Z_{Cg} = (-j5.1)\Omega$, and $Z_{Lg} = (j77.4)\Omega$. The feed line impedance is assumed to be purely resistive, that is $Z_{F2} = 100 \Omega$, and $Z_{F1} = 50 \Omega$. Applying these impedance values to the above equations, the $Z_g = (j26)$, $Z_{UP} = Z_{DW} = (2.83 - j31.81)\Omega$, $Z_L = (9.23 - j39.69)\Omega$, $Z_{in2} = (5.56 + j2.38)\Omega$ and $Z_{in1} =$

(50.06 - j0.64)Ω. Therefore, the final impedance of the antenna, when looked at from the input of the feed line, is $Z_{in1} = 50 \Omega$ with negligible capacitive impedance in the band of interest, as illustrated in Fig. 7(b). Thus, the antenna is tuned to resonate at 38.5 GHz.

III. ARRAY ANTENNA

A planar antenna can use either series, parallel, or hybrid feed. For our case, we choose parallel feed. Generally, the array antenna gain depends on the number of radiating elements arranged in the x-axis (M) or y-axis (N) for the linear array and in both axis for the planar array, which can be computed as,

$$Gain_{Array} = Gain_{SE} + 10\log_{10}(M \times N) \quad (25)$$

where $Gain_{SE}$ is the gain of the single-element antenna. For example, in [33] and [34], a linear 5-element and 4-element array is proposed, which could achieve a maximum gain of 11.6 dBi and 6.7 dBi. Consequently, to enhance the gain further and to attain dual-beam characteristics, we chose a slightly large 4 × 4 array pattern with different spacing for the x-axis and y-axis. Theoretically, from Equation (25), for a 4 × 4 array and for a single-element gain of 7.7 dBi, the array gain would be 19.74 dBi. However, due to the distribution of radiating energy into dual beams and considering feed line losses, the achieved maximum gain is 16.7 dBi, which is relatively acceptable.

The proposed 4 × 4 array antenna is shown in Fig. 8. At first, a 2 × 1 array is constructed with a set of mirrored single-element antennas fed by a 50 Ω feed line. The distance between these two elements dx is 0.77λ (at 38.5 GHz), which is close to $\frac{3}{4}$ of wavelength. Further, the design is expanded to a 2 × 2 array. Here, the horizontal spacing is strategically chosen to achieve dual beam characteristics, as a result, the dy is chosen as 1.16λ , which is close to one wavelength. A 2 × 2 array is expanded to a 4 × 4 array. The initial feed network for a 2 × 2 and 4 × 4 array is designed using the circuit simulator. The two mirrored single-element antenna has input impedance (Z_{in1}) of 50 Ω, consequently, the total impedance of these parallel elements (Z_{pt}) is found to 25 Ω using Equation (26).

$$Z_{pt} = \frac{Z_{in1} Z_{in1}}{Z_{in1} + Z_{in1}} \quad (26)$$

To deliver -3 dB power equally to these elements and to match the impedance between Z_{pt} and Z_2 of 100 Ω, a Z_1 impedance of 50 Ω with a length of $\lambda_g/4$ (where λ_g is the guided wavelength at 38.5 GHz) is chosen because $Z_1 = \sqrt{Z_{pt} Z_2} = 50 \Omega$. Further, to split power on Z_2 lines of 100 Ω, whose parallel impedance resulted in 50 Ω using Equation (23), another impedance arm A3 with Z_3 impedance of 50 Ω is used. Later, to match the impedance of Z_3 (50 Ω) and Z_5 (100 Ω), a quarter-wave transform with 70.7 Ω (Z_4) is added. The rest of the FN is symmetric, which means the impedance of A3, A6, and A9 has an impedance of Z_1 , and A5 and A8 has impedance Z_2 . The FN arm A4 and A7 are quarter-wavelength transforms with impedance 70.7 Ω, to

deliver the power from the 100 Ω feed line to the 50 Ω feed line.

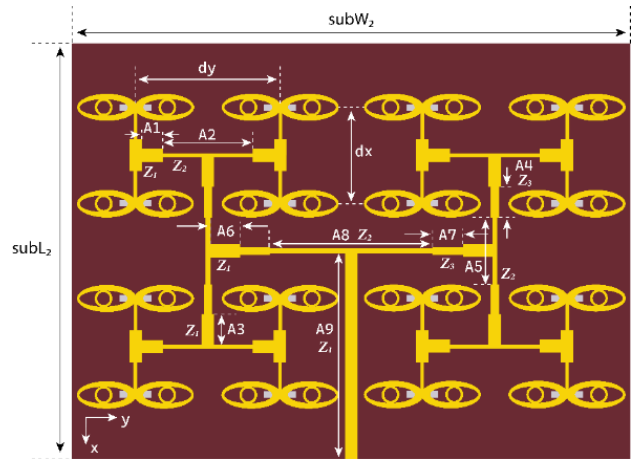


FIGURE 8. Proposed 4 × 4 array antenna with corporate feed network. The dimension in mm as follows: $dy = 9$, $dx = 6$, $A1 = 1.31$, $A2 = 5.6$, $A3 = A4 = A6 = A7 = 1.88$, $A5 = 4.25$, $A8 = 10.25$, $A9 = 12.88$, $subW_2 = 35$, and $subL_2 = 26$.

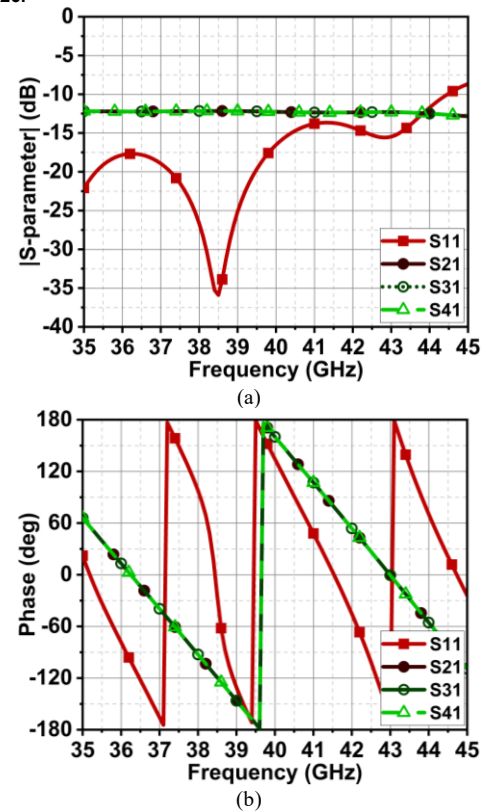


FIGURE 9. Power and phase distribution of proposed feed network structure.

The power distribution and phase response of the feed network are obtained from the circuit simulator, as illustrated in Fig. 9. The results from the circuit simulator illustrate that the tuned FN delivers equal power and phase to all the radiating elements in the band of interest. The $|S_{11}|$ indicates the FN is tuned at a resonance frequency of 38.5 GHz, delivering 98% of power to the radiating elements. From Fig. 9(a), $|S_{21}|$ to $|S_{41}|$ (due to brevity in Fig. 9, only $|S_{21}|$ to

|S41| is demonstrated) is -12.1 dB, meaning each element is delivered with 0.061 W of power for an input power of 1 W. This accounts for 97.6% of power; the remaining 2.4% of power is lost due to feed network and conductivity losses. Nonetheless, the feed network is tuned to its maximum.

From the feed network design, the arm lengths of A1, A3, A4, A6 and A7 are $\lambda_g/4$, where λ_g is a guided wavelength at 38.5 GHz. However, the results are unsatisfactory when the antenna elements are embedded with the designed FN. Thus, the feed network is re-tuned with the antenna element connected. During this process, it is found that suitable arm length (l) of A1, A3, A4, A6, and A7 falls in the range of $\lambda_g/4 > l < \lambda/4$ (where λ is at 38.5 GHz). This is because the circuit simulator does not take into account the minor mismatch from the antenna; as a result, the |S11| graph from the circuit simulator and 3D solver differs. The surface current distribution of the tuned array antenna is shown in Fig. 10. With the array antenna, the bandwidth is increased with two resonance points compared to the single-element antenna. The array antenna has resulted in bandwidth ranging from 36.76-39.92 GHz, which is 8.4% of fractional bandwidth (FB), with resonance at 37.35 GHz and 39.45 GHz, as illustrated in Fig. 11.

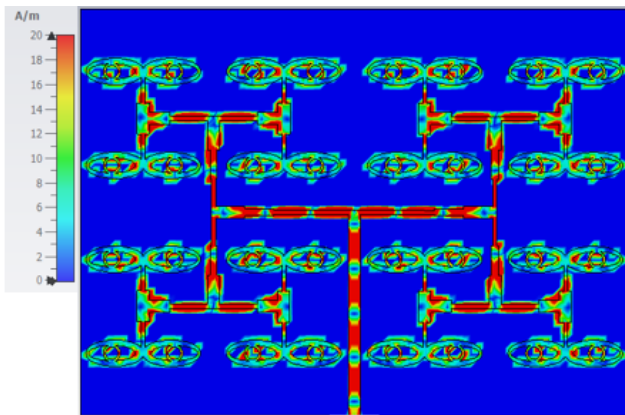


FIGURE 10. Surface current distribution of proposed array antenna at 37.4 GHz.

The array factor for the above-given planar structure is,

$$AF(\theta, \varphi) = \sum_{m=0}^{M-1} \sum_{n=0}^{N-1} e^{j(mkdx \sin(\theta) \cos(\varphi) + nkdy \sin(\theta) \cos(\varphi))} \quad (27)$$

where k is the wavenumber, M and N are the number of radiating elements along the x -axis and y -axis. For $M = N = 4$, the above Equation simplifies to,

$$AF((\theta, \varphi) = \frac{\sin(2kdx \sin(\theta) \cos(\varphi))}{\sin(kdx \sin(\theta) \cos(\varphi))} \times \frac{\sin(2kdy \sin(\theta) \sin(\varphi))}{\sin(kdy \sin(\theta) \sin(\varphi))} \quad (28)$$

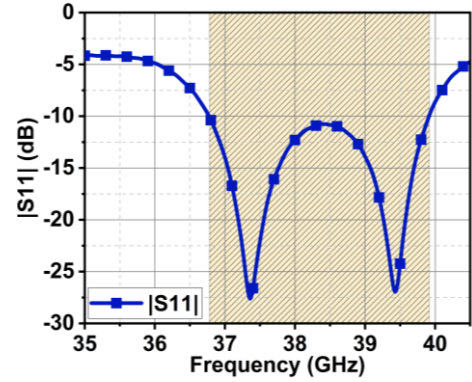
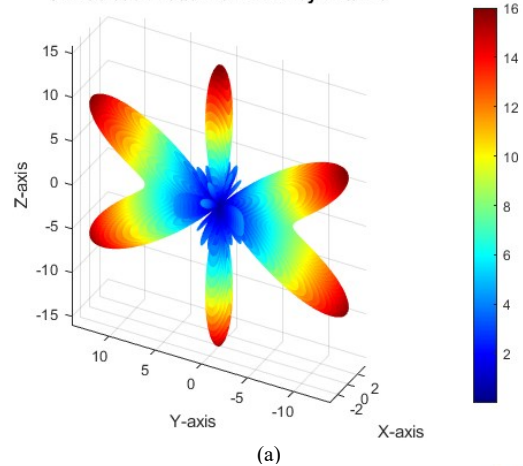
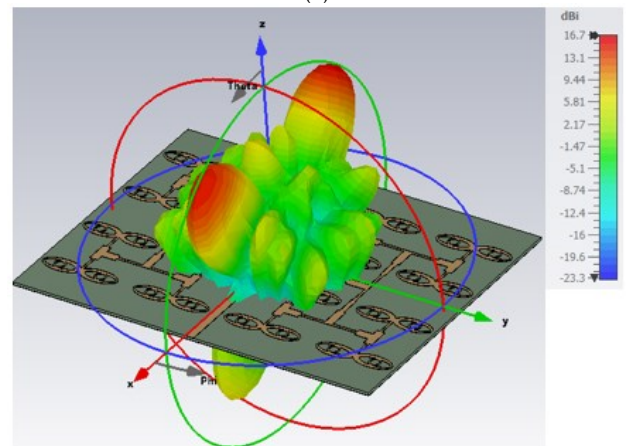


FIGURE 11. Simulated reflection coefficient |S11| results of proposed array antenna.

3D Radiation Pattern of 4x4 Array Antenna



(a)



(b)

FIGURE 12. (a) Estimated and (b) simulated radiation pattern of proposed array antenna at 37.4 GHz.

Using the above Equation, the radiation pattern estimates penta-beam, with two in the broadside direction, that in $+Z$ -axis, and two in the backward direction, that in $-Z$ -axis. The other two beams are parallel to the plane. The estimated gain is 16 dBi with a broadside half-power-beamwidth (HPBW) of 16° . On the contrary, the simulated results demonstrate a quad beam radiation pattern, two on the $+Z$ -axis and two on the $-Z$ -axis (with relatively low intensity), as illustrated in Fig. 12. The back radiation is due to the slot in the ground

plane, which used to tune the antenna resonance and bandwidth. For 5G applications, the preferred beam is a broadside pattern with low back radiation. Thus, with the careful design of the ground plane and the strategic positioning of the slot, the directivity in the back direction is reduced to a certain level, which is comprehended by observing the gain intensity plot in Fig. 13.

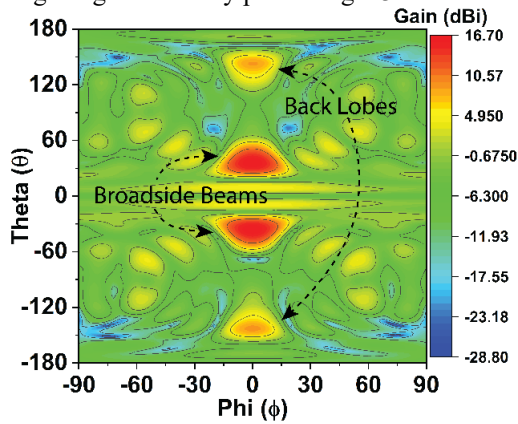


FIGURE 13. Gain intensity plot of the array antenna in the far-field region at 37.4 GHz.

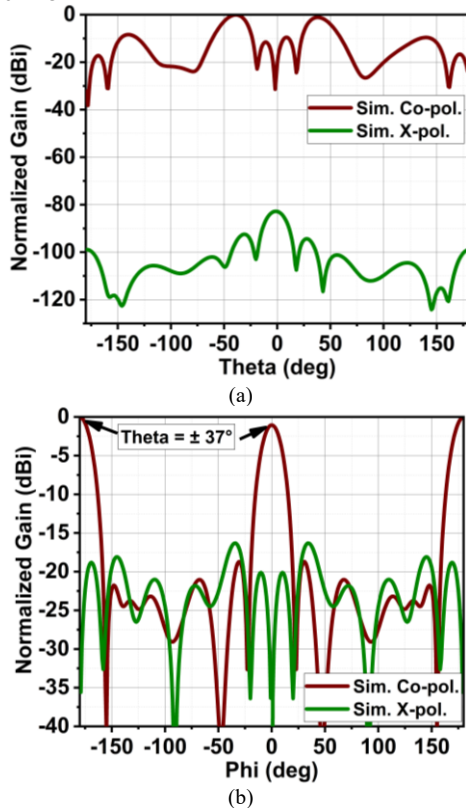


FIGURE 14. Normalized radiation pattern of proposed array antenna at (a) $\varphi = 0^\circ$ and (b) orthogonal plane at $\theta = \pm 37^\circ$ at 37.4 GHz.

The two beams formed in the broadside direction (+Z axis) are at $\pm 37^\circ$ have an HPBW of 22° at $\varphi = 0^\circ$, and HPBW of 18° at $\theta = 37^\circ$. At $\varphi = 0^\circ$, the array antenna has achieved excellent X-polarization of -82.85 dB with a side-lobe level (SLL) of -10 dB. In the orthogonal plane and $\theta = 37^\circ$, the

X-polarization is -16.5 dB with an SLL of -18 dB, as shown in Fig. 14. The array antenna has achieved a maximum gain of 16.7 dBi and an average total efficiency of 90% , as illustrated in Fig. 15.

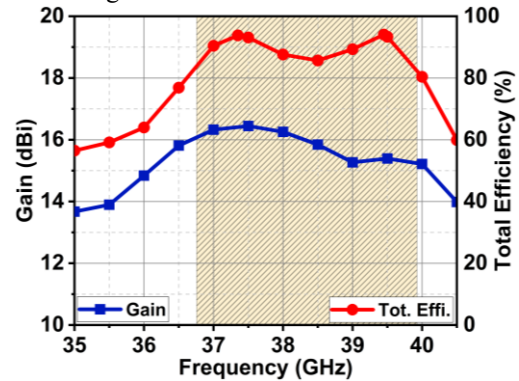


FIGURE 15. Simulated gain and total efficiency results of the proposed array antenna.

IV. MIMO ANTENNA

The MIMO antenna in wireless communication improves the signal-to-noise ratio (SNR) through spatial diversity and increases the channel capacity through spatial multiplexing techniques. The spatial diversity also addresses the issue of the multipath effect, which is severe in the urban scenario, and the signal attenuation due to high path loss at the millimeter wave spectrum. To strengthen the MIMO antenna performance, the above-designed high gain array antenna structure is transformed into a MIMO antenna with two different orientations, one with spatial diversity and the second with pattern diversity. Both orientations are significant in massive MIMO antenna structures. Also, they provide the flexibility to scale the antenna to any number of MIMO antenna ports. The two MIMO orientation structures with four ports are shown in Fig. 1. The dimensions of spatial diversity and pattern diversity structures are $3.35\lambda \times 18.35\lambda$ and $6.42\lambda \times 9.12\lambda$ (at 38.5 GHz), respectively.

The major concern of the MIMO antenna is the mutual coupling. The coupling are broadly classified into three categories: (a) space-wave coupling – caused by a wide-beam radiation pattern interfering with adjacent MIMO element pattern. For our case, the dual-beams are narrow and are in the broadside direction; consequently, the likelihood of space-wave coupling is minimal. (b) Surface-wave coupling – where the wave travels through substrates to adjacent ports, thus degrading the MIMO performance. In our case, the elliptical and circular ring radiating structure and strategically etched ground slot confine the surface wave current, thus refraining it from propagation to adjacent radiating elements. The surface wave current distribution in Fig. 16 proves the significance of structural design in achieving good isolation. The design is so robust that the MIMO antenna with the middle port excited also confines the coupling current to adjacent elements. Likewise, the proposed MIMO antenna in pattern diversity structure also

exhibits good isolation between the elements, as illustrated in Fig. 16(b). (c) Near field effect – causes significant impact when MIMO antenna port-to-port distance is less than operating wavelength. Due to the MIMO array configuration in the proposed structures, the port-to-port distance is sufficiently large to maintain a low near-field effect.

The reflection coefficient resulting from both designs aligns with the results of the array antenna structure. Thus, spatial and pattern diversity structure has bandwidth ranging from 36.77-39.93 GHz and 36.77-39.91 GHz, which constitutes 8.4% of FB. It is worth noting that the isolation $|S_{21}|$ is > 31 dB in spatial diversity structure, and it increases with an increase in distance for $|S_{31}|$ and $|S_{41}|$ reaching > 50 dB and > 66 dB. In the case of pattern diversity structure, the isolation to an adjacent element $|S_{21}|$ is > 31.2 dB, for the opposite element $|S_{31}|$ is > 30.4 dB, and for diagonal element $|S_{41}|$ is > 38 dB, as illustrated in Fig. 17.

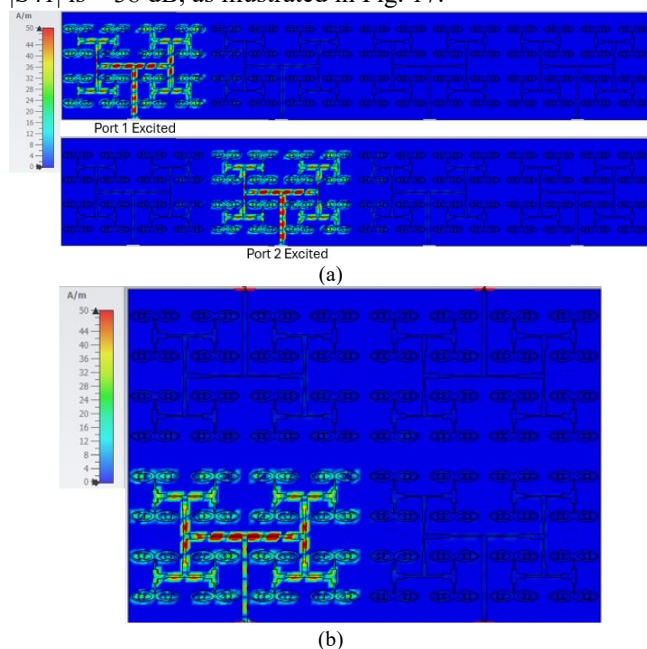


FIGURE 16. Surface current distribution of proposed MIMO antenna of (a) spatial diversity structure and (b) pattern diversity structure.

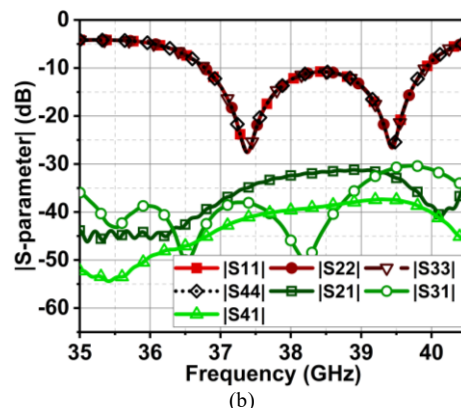
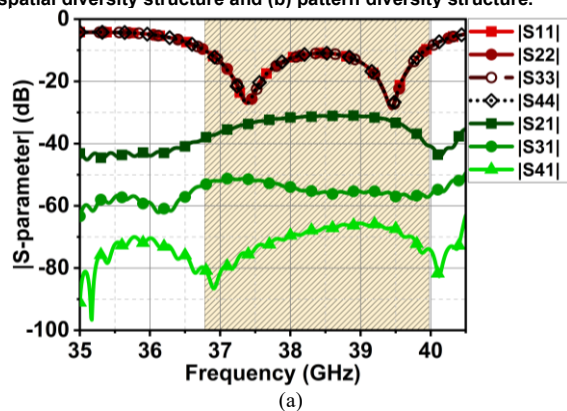


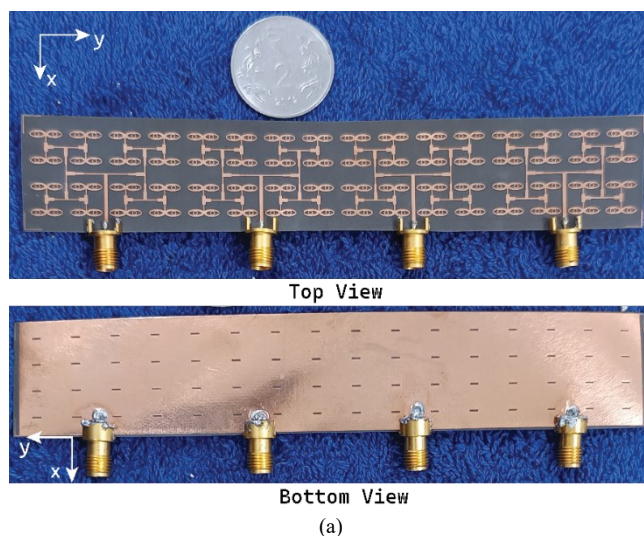
FIGURE 17. Simulated $|S\text{-parameter}|$ results of (a) spatial diversity structure and (b) pattern diversity structure of proposed MIMO antenna.

The isolation results indicate the structure is robust and can be used in any configuration. Both structures have resulted in a dual-beam radiation pattern in broadside at an elevation angle of $\pm 37^\circ$ with a gain of 16.9 dBi and 16.7 dBi, respectively.

V. RESULTS AND DISCUSSION

A. $|S\text{-parameter}|$ and Radiation Pattern

The simulated results of the MIMO antenna are validated by measuring the prototype fabricated antenna, and its measurement setup is shown in Figs. 18 and 19. A 2.92 mm end launch connector from Johnsons is used to feed the signal to the antenna. The $|S\text{-parameter}|$ and radiation pattern are measured using a vector network analyzer (VNA) from Anritsu S820E (1 MHz-40 GHz). With the spatial diversity MIMO antenna, the simulated $|S_{11}| \geq 10$ dB is from 36.77-39.93 GHz, and the measured is from 36.4-40* GHz. The simulated $|S_{21}|$, $|S_{31}|$, and $|S_{41}|$ are > 31 dB, > 51 dB, and > 66 dB in the band of interest.



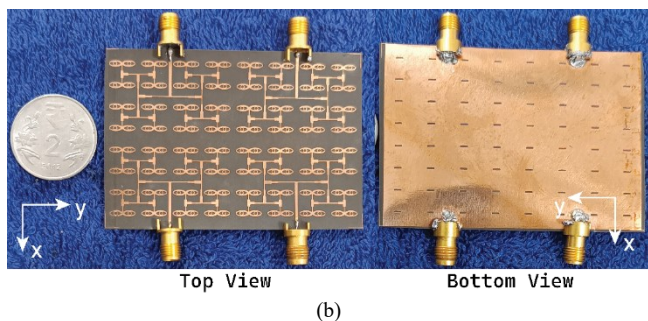


FIGURE 18. Prototype fabrication of MIMO antenna. (a) Spatial diversity structure, and (b) pattern diversity structure.

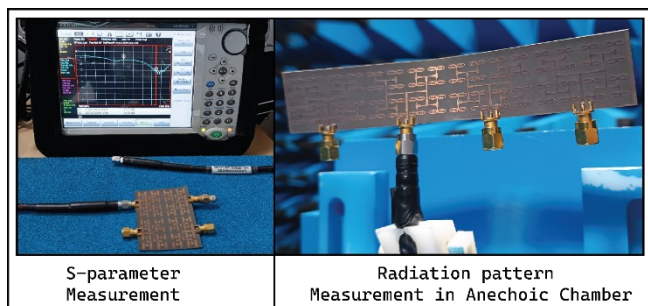


FIGURE 19. Measurement setup of |S-parameter| using Anritsu S820E VNA (1 MHz – 40 GHz) and radiation pattern in an anechoic chamber.

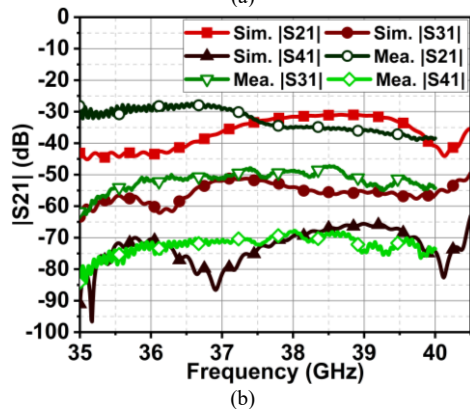
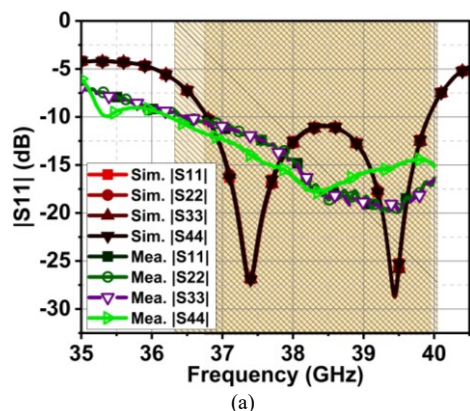


FIGURE 20. Simulated and measured (a) reflection coefficient |S11| and (b) transmission coefficient |S21| of spatial diversity MIMO antenna structure.

The respective measured isolations are > 29 dB, > 47 dB, and > 69 dB, as depicted in Fig. 20. For the case of pattern diversity, the simulated and measured reflection coefficient $|S_{11}| \geq 10$ dB is 36.77-39.91 GHz and 35.7-40* GHz, respectively. The simulated and measured isolation $|S_{21}|$ is > 31.2 dB, $|S_{31}|$ is > 30.4 dB, and $|S_{41}|$ is > 38 dB, as shown in Fig. 21. The * indicates the limitation of the instrument measuring capacity only up to 40GHz. The measured reflection coefficient indicates the existence of bandwidth > 40 GHz; following the pattern, it can reach up to 41 GHz.

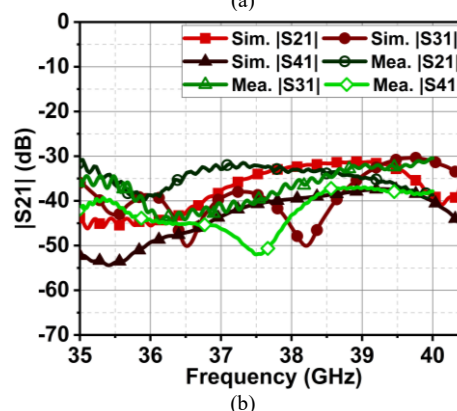
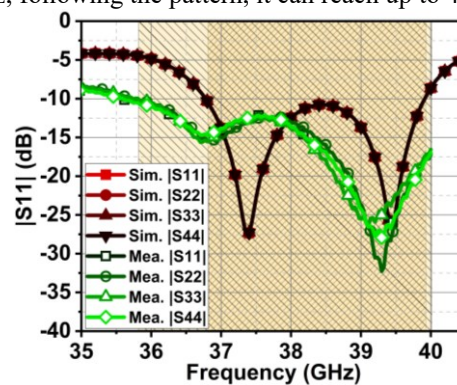


FIGURE 21. Simulated and measured (a) reflection coefficient |S11| and (b) transmission coefficient |S21| of pattern diversity MIMO antenna structure.

The measured results of pattern MIMO and spatial MIMO structure demonstrated discrepancies from the simulated results. The primary reason for deviation in results, particularly for spatial MIMO antenna, is because of the thin substrate and its wide width relative to its length. When this structure is fed to the fabrication machine, its shape is deformed due to the thermal effect and wide rectangular dimension, resulting in a bent shape, as the Fig. 22(a) illustrating the flexible nature of the antenna. The spatial MIMO antenna is modeled in electromagnetic solvers, bending at 30° and 50° to study this effect, as depicted in Fig. 22(b). However, with the available 64 GB RAM and i7 processor, the simulation system ran out of memory due to large structure and complex meshing. Consequently, the bending effect is performed on an array antenna at 30° and

50°, as it is relatively smaller in size and takes less memory for meshing and computation.

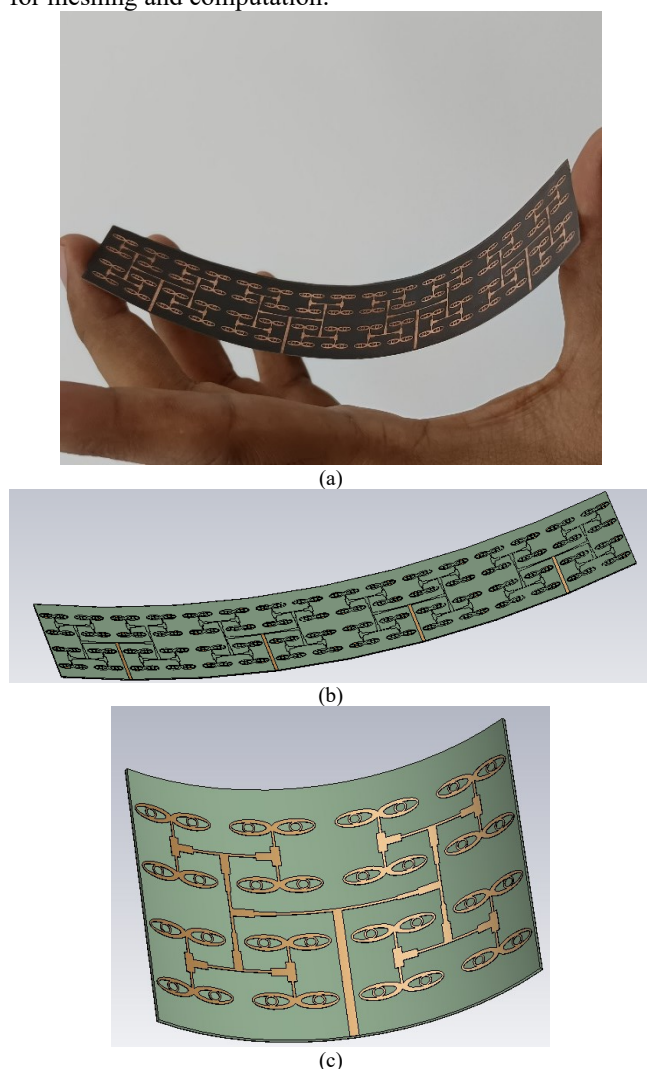


FIGURE 22. Illustrating the bending effect due to the thin substrate and wide antenna dimension. (a) Bending of fabricated spatial MIMO antenna. (b) and (c) Modeling bend of spatial MIMO antenna and array antenna in electromagnetic solver.

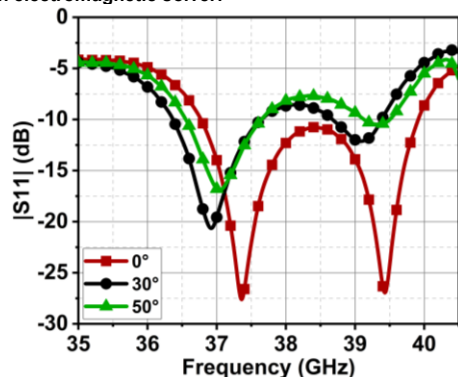


FIGURE 23. Simulated results of array antenna bending at 0°, 30° and 50°.

The simulation results in Fig. 23 depict that the bending leads to poor impedance matching at higher frequencies,

thereby reducing the operational bandwidth. However, in our case, the measured operation bandwidth is larger for spatial and pattern MIMO antenna than the simulated results. Other possible reasons for deviation in results may be due to fabrication tolerance, port connection, or manual soldering, which may sometimes cause dry soldering. Nonetheless, the measured operating bandwidth of both pattern and spatial MIMO structures covers the simulated results.

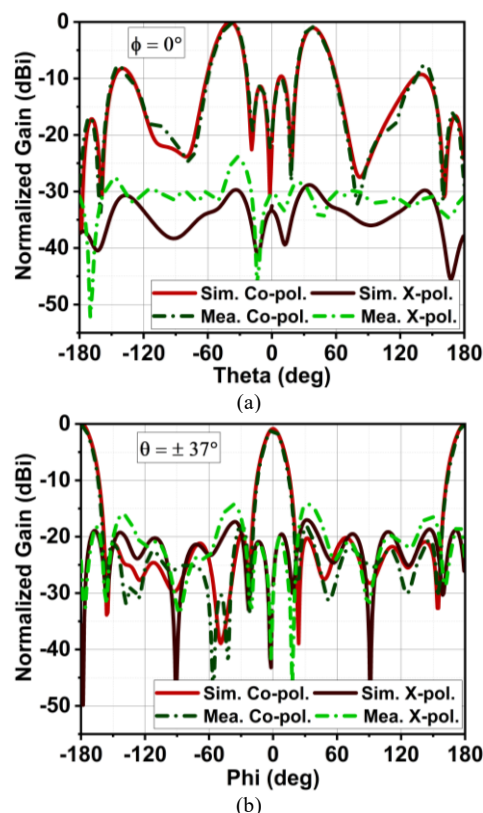
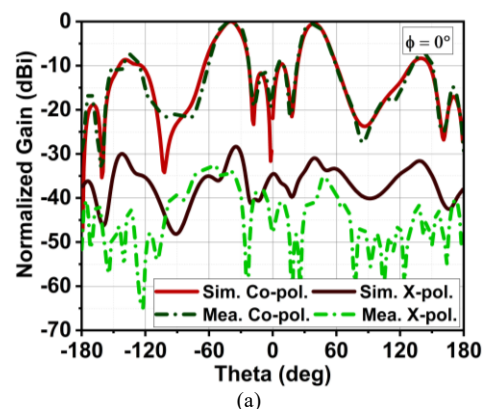


FIGURE 24. Simulated and measured radiation pattern of spatial diversity MIMO antenna at (a) xz -plane ($\phi = 0^\circ$) resulting in a dual narrow beam at 37° . (b) Representing the beam in another plane that is in yz -plane ($\theta = \pm 37^\circ$).



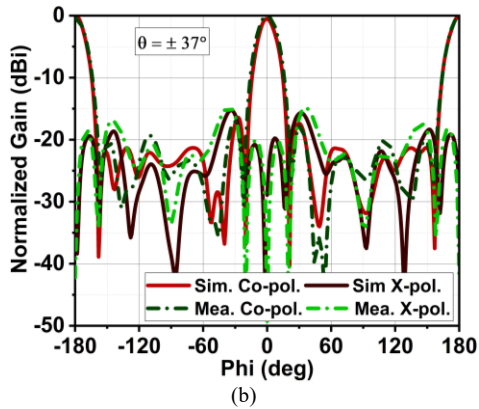


FIGURE 25. Simulated and measured radiation pattern of pattern diversity MIMO antenna at (a) xz-plane ($\varphi = 0^\circ$) resulting in a dual narrow beam at 37° . (b) Representing the beam in another plane that is in yz-plane ($\theta = \pm 37^\circ$).

The spatial diversity MIMO antenna generates a dual beam in a broadside direction at an angle of $\theta = \pm 37^\circ$. At $\varphi = 0^\circ$ plane, the simulated and measured HPBW is 21° and 20° , as shown in Fig. 24(a). The SLL is at -10 dB, whereas simulated and measured X-polarization is at -28 dB and -24 dB, respectively. In the orthogonal plane and at $\theta = \pm 37^\circ$, the simulated and measured HPBW is 17.5° and 14.5° , SLL is -20 dB and -18 dB, and X-polarization is -17.5 and -14.5 dB, respectively, as illustrated in Fig. 24(b).

The radiation characteristics of pattern diversity MIMO antenna are almost identical to spatial structure. At $\varphi = 0^\circ$, the simulated and measured HPBW is 20° and 25° , with SLL of -10 dB and X-polarization of -28.5 dB and -33 dB, respectively, as illustrated in Fig. 25(a). In the other plane, at $\theta = \pm 37^\circ$, simulated and measured HPBW is 16° and 18° , with SLL of -17.5 dB and X-polarization of -15 dB, as shown in Fig. 25(b). For both the diversity MIMO antenna structures, the maximum achieved gain is 16.7 dBi with an average total efficiency of 83.8% in the band of interest, as depicted in Fig. 26.

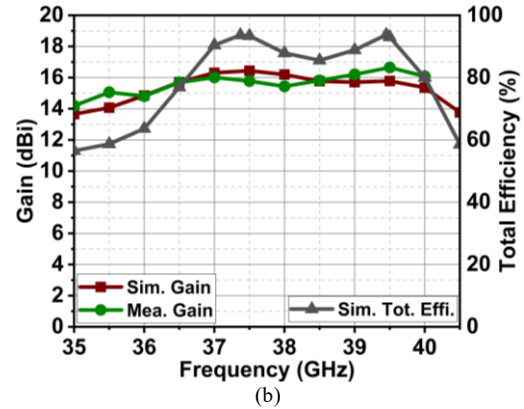
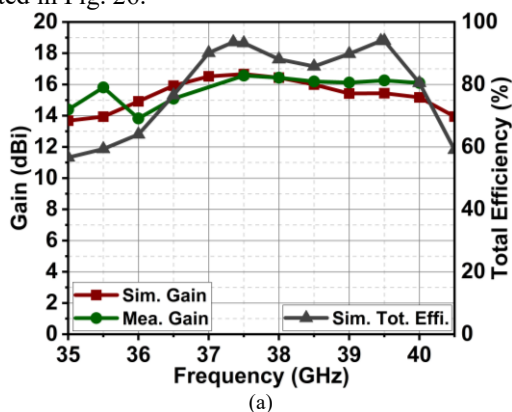


FIGURE 26. Simulated and measured gain plot of (a) spatial diversity and (b) pattern diversity MIMO antenna with its simulated total efficiency response.

B. Diversity Metrics

This section validates the MIMO antenna performance through diversity metrics such as ECC, DG, CCL, and TARC. The MIMO antenna with good decoupling mechanisms causes reduced mutual coupling and correlation of signal between the antenna elements. As a result, the ECC will lower. The ECC can be computed with the $|S\text{-parameter}|$ (Equation (3) in [35]) or through a far-field radiation pattern (Equation (4) in [35]). The far-field radiation pattern provides a much more accurate relation of the correlation of received signals. Thus, far-field patterns are used to compute the ECC for our case. For the spatial diversity MIMO antenna, the ECC is < 0.05 ; for the pattern diversity antenna, the ECC is < 0.1 in the band of interest, a slight increase due to the opposite element minor coupling. Nonetheless, both antenna structures offer excellent low correlation, thus enhancing the spatial multiplexing and overall throughput. The diversity gain is dependent on ECC; ideally, it must be 10. For both the MIMO structures, the DG is > 9.99 , as shown in Fig. 27.

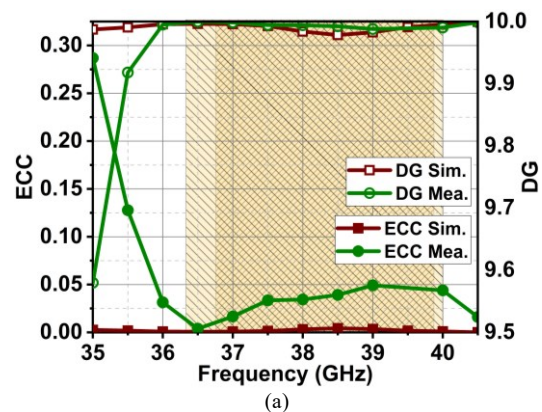


TABLE I
COMPARISON OF THE PROPOSED MIMO ANTENNA WITH STATE-OF-THE-ART DESIGNS.

Ref	Dim. in mm ³	Dim. in λ_1^3	Res. (GHz)	Ant. Type	No. of Ports	No. of lay.	FN	BW	Iso. S21	Gain (dBi)	Avg. Totl. Effe. (%)
[37]	60 × 35.7 × 0.5	8.5 × 5 × 0.063	42/55	LWA	2	1	Ser.	41-53/50-65	> 28/ 16	18.6/ 19.6	70/ 63
[38]	125.3 × 125.3 × 3.2	11.7 × 11.7 × 0.3	28	LWA	2	4	SIW	27.6-29.5	> 51	23.5	NAV
[39]	20 × 45 × 0.83	2 × 4.5 × 0.083	30	ME	2	2	MS	25.3-31.5	> 21.5	6	
[40]	12 × 50 × 0.8	1.12 × 4.67 × 0.075	28	Planar patch	2	1	Planar Cor.	25.2-29.4	> 30	11.5	90
[41]	20 × 40 × 0.254	2.57 × 5.14 × 0.035	38	Planar patch	2	1	Planar Cor.	38.35-38.66	> 40*	12.8	85
[42]	16 × 26 × 0.254	1.5 × 2.43 × 0.024	28	Planar Mono	2	1	Planar Cor.	26.1-34	> 20	7.15	93*
[43]	31.8 × 60.6 × 0.5	2.91 × 5.66 × 0.05	28	Planar patch	4	1	Planar Cor.	27-28.5	> 30*	12.5	89
[44]	46 × 46 × 0.58	4.3 × 4.3 × 0.054	28	Planar patch	4	4	Planar Cor.	26.31-30.25	> 34*	11.7	83
[45]	150 × 80 × 0.8	2.4 × 1.28 × 0.013	4.8/28	Planar Dipole	8	1	NA	4.7-4.9/28.3-29	> 14/ 26	4.9/ 7.2	87/ 88
Prop. Spat.	26 × 143 × 0.254	3.35 × 18.35 × 0.03	38.5	Planar patch	4	1	Planar Cor.	36.4-40*	> 29	16.7	83.8
Prop. Patt.	50 × 71 × 0.254	6.42 × 9.12 × 0.03	38.5	Planar patch	4	1	Planar Cor.	35.7-40*	> 31.2	16.7	83.8

MS – microstrip feedline, isolation with * indicates the antenna structures are in orthogonal orientation to give better isolation. Dim.-dimension, Res.-resonance, FN-feed network, BW-bandwidth, Iso.-isolation, Avg. Tot. Effe.-average total efficiency, Ser.-series, Cor.-corporate feed

TABLE II

COMPARISON OF THE PROPOSED MIMO ANTENNA WITH STATE-OF-THE-ART DESIGNS WITH RESPECT TO RADIATION PATTERN AND DIVERSITY METRICS.

Ref.	No. of Beams in Broadside	xz-plane			yz-plane			Diversity Metrics			
		HPBW	X-pol.	SLL	HPBW	X-pol.	SLL	ECC	DG	CCL b/s/Hz	TARC at -10 dB
[37]	Dual	At ($\theta = 15^\circ$) 20.4°/ 12°	At ($\theta = 15^\circ$) 25	< -15	76°/ 80°	NAV	NAV	NA	NA	NA	NA
[38]	Single	06°	35	< -12.5	08°	29	< -20	NA	NA	NA	NA
[40]	Single	NAV	NAV	NAV	40°	NAV	< -5	< 0.4E-4*	> 9.99	NAV	NAV
[41]	Single	22°	NAV	< -11.7	68.2°	NAV	< -24	< 1E-4*	> 9.99	0.15	NAV
[42]	Bi-direc.	66°	NA	NA	50°	NA	NA	< 0.25E-3*	> 9.99	0.4	27-33
[43]	Single	19.8°	NAV	< -5.6	51.2°	NAV	< -21.5	< 0.4E-4*	> 9.99	0.45	NAV
[44]	Single	60°	22	< -12	78°	NAV	< -17	< 0.2E-3	> 9.99	NAV	26.3-28.5
[45]	Omni	-	-	-	-	-	-	< 0.02*	> 9.99	-	4.78-4.85/ 28.4-29
Prop. Spat.	Dual	20°	24	< -18	At ($\theta = \pm 37^\circ$) 14.5°	14.5	< -18	< 0.05	> 9.99	0.26	36.75-40*
Prop. Patt.	Dual	25°	33	< 10	At ($\theta = \pm 37^\circ$) 18°	15	< 17.5	< 0.1	> 9.99	0.26	35.7-40*

The ECC with * indicates the designs used approximate method to estimate.

The loss in the communication channel due to MIMO antenna mutual coupling and correlation between antenna is measured through channel capacity loss (CCL) using equations defined in [36]. The acceptable threshold limit is 0.4 b/s/Hz. Both structures have resulted in simulated and measured CCL of 0.26 b/s/Hz, less than the threshold limit. The TARC estimates the ratio of power delivered to the load to the incident power by considering all the MIMO elements simultaneously. The higher the reflections from the load, the higher the TARC, thus degrading the MIMO antenna performance. The simulated and measured TARC is ≤ -10 dB for the band of interest, as shown in Fig. 28. The performance comparison of proposed MIMO antenna structures with other designs is summarized in Tables 1 and 2.

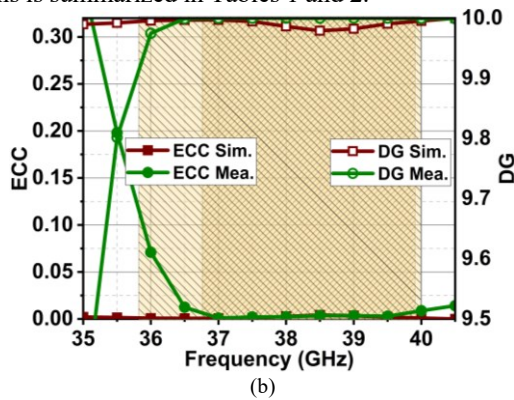


FIGURE 27. Simulated and measured ECC and DG using the far-field method. (a) Spatial diversity MIMO antenna. (b) Pattern diversity MIMO antenna.

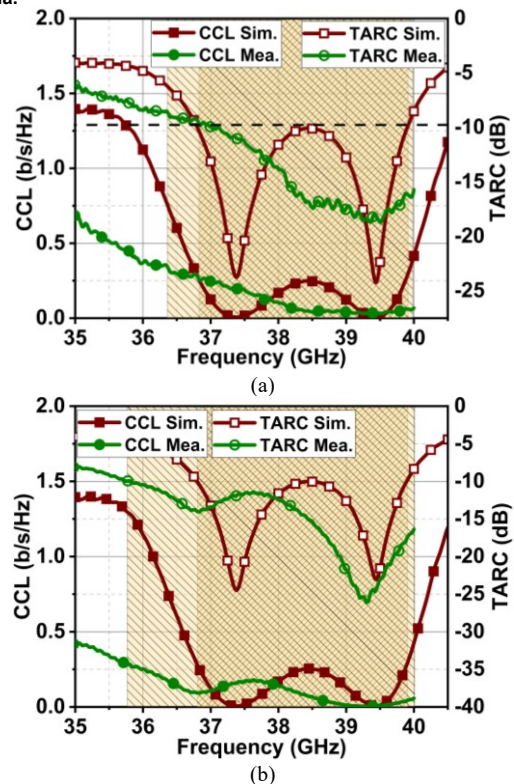


FIGURE 28. Simulated and measured CCL and TARC. (a) Spatial diversity MIMO antenna. (b) Pattern diversity MIMO antenna.

C. Beam Steering

Both the proposed MIMO antenna structures offer some degree of beam steering ability when used with the beam forming network (BFN). The design of BFN is beyond the scope of this article, however, by changing the phase at the ports of the MIMO antenna, beam steering ability is achieved.

With all four ports of the spatial MIMO antenna excited with zero phase, the beam is further narrowed in one of the planes, and the gain increases to 23 dBi. In xz -plane ($\varphi = 0^\circ$), the HPBW is similar to single-port excitation, that is, 21° , with exceptionally low X-polarization of -78 dB. The achieved SLL is -10 dB. However, in the orthogonal plane and $\theta = \pm 37^\circ$, the radiation pattern forms a constructively narrow beam of 4.5° , with SLL of -15 dB and X-polarization of -22 dB, as depicted in Figs. 29(a) and 29(b).

Likewise, when all four ports of pattern diversity MIMO antenna are excited, the constructive pattern narrows the beam in both planes, as a result, a narrow of 11° and 09° HPBW at $\varphi = 0^\circ$ and in the other plane at $\theta = \pm 37^\circ$ are achieved, with an X-polarization of -79 dB and -23 dB, respectively. The SLL at both planes is -9 dB and -14 dB, as illustrated in Fig. 30.

As an example, the beam steering of the spatial MIMO antenna is demonstrated in Fig. 31 for relatively different phases at the antenna ports. Here, cases 1 and 4 achieved beam steering at $\pm 02^\circ$, and cases 2 and 3 achieved beam steering at $\pm 07^\circ$.

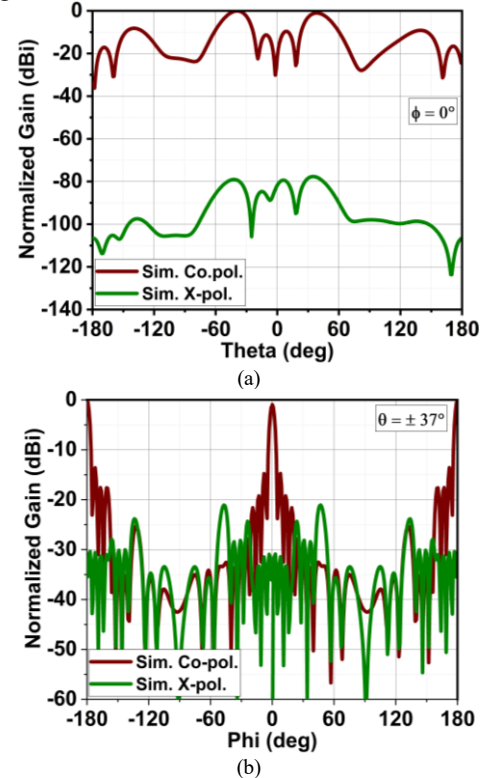


FIGURE 29. Radiation pattern of spatial diversity MIMO antenna when all four ports are excited with zero phase. (a) Pattern in the $\varphi = 0^\circ$ plane, and (b) pattern in the other plane at $\theta = \pm 37^\circ$.

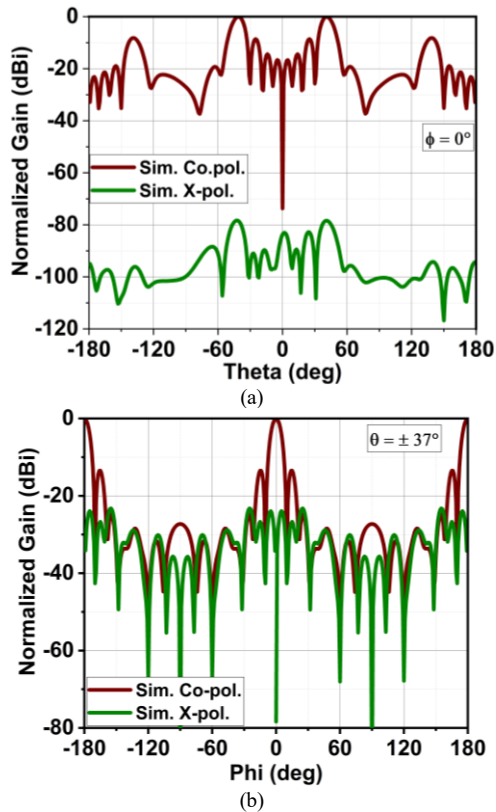


FIGURE 30. Radiation pattern of pattern diversity MIMO antenna when all four ports are excited. (a) Pattern in the $\phi = 0^\circ$ plane, and (c) pattern in the other plane at $\theta = \pm 37^\circ$.

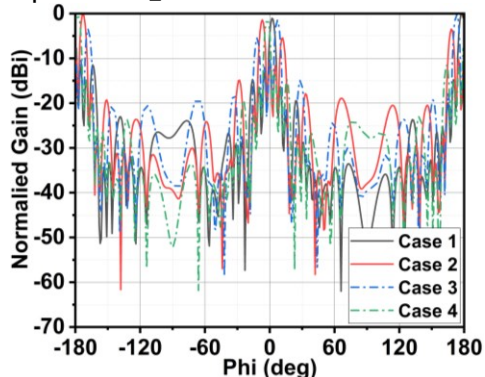


FIGURE 31. Demonstrates the beam steering ability by applying relatively different phases for the four ports of spatial MIMO antenna. Case 1 is for phases (-45, -90, -135, -180), case 2 (-135, 0, +135, -90), case 3 (-90, +135, 0, -135), and case 4 (-180, -135, -90, -45).

VI. CONCLUSION

This article presented a novel MIMO antenna design that effectively integrates spatial and pattern diversity structures, achieving superior performance with consistent reflection coefficients and radiation patterns. The innovation lies in the strategic placement of a circular ring in the patch and a slot in the ground plane of the single-element antenna, which successfully generates resonance at the first harmonic frequency of 38.5 GHz. Expanding the design into a 4×4 array further enhances the antenna's performance, improving gain and fractional bandwidth while achieving a narrowed

beam, demonstrating significant advancement over conventional designs. The transformation of the array into spatial and pattern diversity MIMO configurations highlights another key novelty, as these structures achieve robust performance with suppressed mutual coupling and exceptional isolation exceeding 30 dB. The potential for future expansion to an 8×8 array and the incorporation of a beamforming network (BFN) for beam-steering capabilities underscores the adaptability and forward-looking nature of the proposed design. These innovative features make the proposed antenna structures highly suitable for next-generation 5G wireless applications, offering a versatile and high-performance solution for overcoming the challenges of millimeter-wave communication.

REFERENCES

- [1] D. Shakya, S. Ju, O. Kanhere, H. Poddar, Y. Xing, and T. S. Rappaport, "Radio Propagation Measurements and Statistical Channel Models for Outdoor Urban Microcells in Open Squares and Streets at 142, 73, and 28 GHz," *IEEE Trans. Antennas Propagat.*, vol. 72, no. 4, pp. 3580–3595, Apr. 2024, doi: 10.1109/TAP.2024.3366581.
- [2] S. Mohebi, F. Michelinakis, A. Elmokashfi, O. Grondalen, K. Mahmood, and A. Zanella, "Sectors, Beams and Environmental Impact on the Performance of Commercial 5G mmWave Cells: An Empirical Study," *IEEE Access*, vol. 10, pp. 133309–133323, 2022, doi: 10.1109/ACCESS.2022.3229588.
- [3] A. E. C. Redondi, C. Innamorati, S. Gallucci, S. Fiocchi, and F. Matera, "A Survey on Future Millimeter-Wave Communication Applications," *IEEE Access*, vol. 12, pp. 133165–133182, 2024, doi: 10.1109/ACCESS.2024.3438625.
- [4] A. Ramos, T. Varum, and J. N. Matos, "A Review on Mutual Coupling Reduction Techniques in mmWaves Structures and Massive MIMO Arrays," *IEEE Access*, vol. 11, pp. 143143–143166, 2023, doi: 10.1109/ACCESS.2023.3343107.
- [5] P. S. B. G, P. R. Mane, P. Kumar, T. Ali, and M. G. Nabi Alsath, "Planar MIMO antenna for mmWave applications: Evolution, present status & future scope," *Heliyon*, vol. 9, no. 2, p. e13362, Feb. 2023, doi: 10.1016/j.heliyon.2023.e13362.
- [6] W. J. Yang, Y. M. Pan, and S. Y. Zheng, "Mutual Coupling Reduction in CP MIMO Crossed-Dipole Antenna Array," *Antennas Wirel. Propag. Lett.*, vol. 21, no. 12, pp. 2442–2446, Dec. 2022, doi: 10.1109/LAWP.2022.3196371.
- [7] M. Khalid *et al.*, "4-Port MIMO Antenna with Defected Ground Structure for 5G Millimeter Wave Applications," *Electronics*, vol. 9, no. 1, p. 71, Jan. 2020, doi: 10.3390/electronics9010071.
- [8] B. G. P. Shariff, T. Ali, P. R. Mane, P. Kumar, and S. Pathan, "Compact wideband two-element millimeter wave MIMO antenna with CMT based modified T-shaped decoupling structure for mobile applications with estimated link budget in urban scenario," *AEU - International Journal of Electronics and Communications*, vol. 177, p. 155209, Apr. 2024, doi: 10.1016/j.aeu.2024.155209.
- [9] Y. Liu, X. Yang, Y. Jia, and Y. J. Guo, "A Low Correlation and Mutual Coupling MIMO Antenna," *IEEE Access*, vol. 7, pp. 127384–127392, 2019, doi: 10.1109/ACCESS.2019.2939270.
- [10] Z. Wang, C. Li, Q. Wu, and Y. Yin, "A Metasurface-Based Low-Profile Array Decoupling Technology to Enhance Isolation in MIMO Antenna Systems," *IEEE Access*, vol. 8, pp. 125565–125575, 2020, doi: 10.1109/ACCESS.2020.3007188.
- [11] Q. X. Lai, Y. M. Pan, and S. Y. Zheng, "A Self-Decoupling Method for MIMO Antenna Array Using Characteristic Mode of Ground Plane," *IEEE Trans. Antennas Propagat.*, vol. 71, no. 3, pp. 2126–2135, Mar. 2023, doi: 10.1109/TAP.2023.3240561.
- [12] G.-B. Wu, Y.-S. Zeng, K. F. Chan, B.-J. Chen, S.-W. Qu, and C. H. Chan, "High-Gain Filtering Reflectarray Antenna for Millimeter-Wave Applications," *IEEE Trans. Antennas Propagat.*, vol. 68, no. 2, pp. 805–812, Feb. 2020, doi: 10.1109/TAP.2019.2943432.

- [13] L. Malviya and P. Gupta, "Millimeter Wave High-Gain Antenna Array for Wireless Applications," *IETE Journal of Research*, pp. 1–10, Mar. 2021, doi: 10.1080/03772063.2021.1903346.
- [14] Y. Cheng and Y. Dong, "High-Gain All-Metal 3-D Printed Lens-Horn Antenna for Millimeter-Wave Applications," *Antennas Wirel. Propag. Lett.*, vol. 22, no. 2, pp. 308–312, Feb. 2023, doi: 10.1109/LAWP.2022.3209788.
- [15] Z.-Y. Zhang, K. W. Leung, and K. Lu, "Wideband High-Gain Omnidirectional Biconical Antenna for Millimeter-Wave Applications," *IEEE Trans. Antennas Propagat.*, vol. 71, no. 1, pp. 58–66, Jan. 2023, doi: 10.1109/TAP.2022.3216104.
- [16] H. A. Mohamed, M. Edries, M. A. Abdelghany, and A. A. Ibrahim, "Millimeter-Wave Antenna With Gain Improvement Utilizing Reflection FSS for 5G Networks," *IEEE Access*, vol. 10, pp. 73601–73609, 2022, doi: 10.1109/ACCESS.2022.3189651.
- [17] W. Zhao, X. Li, Z. Qi, and H. Zhu, "Broadband and High-Gain High-Order-Mode Fed Open-Ended Waveguide Antenna Array for Millimeter-Wave Applications," *IEEE Trans. Antennas Propagat.*, vol. 70, no. 9, pp. 8614–8619, Sep. 2022, doi: 10.1109/TAP.2022.3168738.
- [18] S. Khan *et al.*, "A Highly Compact Split Ring Resonator-Based Rectangular Dielectric Resonator Antenna With Multiband Characterization," *IEEE Access*, vol. 13, pp. 2360–2376, 2025, doi: 10.1109/ACCESS.2024.3512201.
- [19] S. Khan, O. Khan, S. A. A. Shah, B. T. Malik, N. Gohar, and S. Koziel, "A compact circularly polarized dielectric resonator antenna with MIMO characterizations for UWB applications," *Sci Rep*, vol. 14, no. 1, p. 22627, Sep. 2024, doi: 10.1038/s41598-024-73282-2.
- [20] H. Sarfraz *et al.*, "Next-Generation Multiband Wireless Systems: A Compact CSSR-Based MIMO Dielectric Resonator Antenna Approach," *IEEE Access*, vol. 12, pp. 4910–4924, 2024, doi: 10.1109/ACCESS.2023.3324551.
- [21] D. A. Sehrai *et al.*, "Design of high gain base station antenna array for mm-wave cellular communication systems," *Sci Rep*, vol. 13, no. 1, p. 4907, Mar. 2023, doi: 10.1038/s41598-023-31728-z.
- [22] K. Sultan, M. Ikram, and N. Nguyen-Trong, "A Multiband Multibeam Antenna for Sub-6 GHz and mm-Wave 5G Applications," *Antennas Wirel. Propag. Lett.*, vol. 21, no. 6, pp. 1278–1282, Jun. 2022, doi: 10.1109/LAWP.2022.3164627.
- [23] C. Ma, S. Y. Zheng, Y. M. Pan, and Z. Chen, "Millimeter-Wave Fully Integrated Dielectric Resonator Antenna and Its Multi-Beam Application," *IEEE Trans. Antennas Propagat.*, vol. 70, no. 8, pp. 6571–6580, Aug. 2022, doi: 10.1109/TAP.2022.3161361.
- [24] Y. Zhang, Z. Han, S. Tang, S. Shen, C.-Y. Chiu, and R. Murch, "A Highly Pattern-Reconfigurable Planar Antenna With 360° Single- and Multi-Beam Steering," *IEEE Trans. Antennas Propagat.*, vol. 70, no. 8, pp. 6490–6504, Aug. 2022, doi: 10.1109/TAP.2022.3161514.
- [25] A. A. Ibrahim, W. A. E. Ali, M. Alathbah, and A. R. Sabek, "Four-Port 38 GHz MIMO Antenna with High Gain and Isolation for 5G Wireless Networks," *Sensors*, vol. 23, no. 7, p. 3557, Mar. 2023, doi: 10.3390/s23073557.
- [26] A. R. Sabek, A. A. Ibrahim, and W. A. Ali, "Dual-Band Millimeter Wave Microstrip Patch Antenna with StubResonators for 28/38 GHz Applications," *J. Phys.: Conf. Ser.*, vol. 2128, no. 1, p. 012006, Dec. 2021, doi: 10.1088/1742-6596/2128/1/012006.
- [27] M. H. Sharaf, A. I. Zaki, R. K. Hamad, and M. M. M. Omar, "A Novel Dual-Band (38/60 GHz) Patch Antenna for 5G Mobile Handsets," *Sensors*, vol. 20, no. 9, p. 2541, Apr. 2020, doi: 10.3390/s20092541.
- [28] A. E. Farahat and K. F. A. Hussein, "Dual-Band (28/38 GHz) Wideband MIMO Antenna for 5G Mobile Applications," *IEEE Access*, vol. 10, pp. 32213–32223, 2022, doi: 10.1109/ACCESS.2022.3160724.
- [29] P. Liu, X.-W. Zhu, Y. Zhang, X. Wang, C. Yang, and Z. H. Jiang, "Patch Antenna Loaded With Paired Shorting Pins and H-Shaped Slot for 28/38 GHz Dual-Band MIMO Applications," *IEEE Access*, vol. 8, pp. 23705–23712, 2020, doi: 10.1109/ACCESS.2020.2964721.
- [30] K. C. Ravi and J. Kumar, "Multi-directional Wideband Unit-element MIMO Antenna for FR-2 Band 5G Array Applications," *Iran J Sci Technol Trans Electr Eng*, vol. 46, no. 2, pp. 311–317, Jun. 2022, doi: 10.1007/s40998-022-00486-5.
- [31] K. C. Ravi and J. Kumar, "Miniaturized Parasitic Loaded High-Isolation MIMO Antenna for 5G Applications," *Sensors*, vol. 22, no. 19, p. 7283, Sep. 2022, doi: 10.3390/s22197283.
- [32] C. A. Balanis, *Antenna theory: analysis and design*, Fourth edition. Hoboken, New Jersey: Wiley, 2016.
- [33] N. R. Palepu and J. Kumar, "Neutralized meander line patch antipodal vivaldi defected ground millimeter-wave (mm-wave) antenna array," *AEU - International Journal of Electronics and Communications*, vol. 166, p. 154663, Jul. 2023, doi: 10.1016/j.aeue.2023.154663.
- [34] N. R. Palepu, J. Kumar, S. Peddakrishna, and A. Ghosh, "Wideband meander-line-antipodal-vivaldi slot-antenna for millimeter-wave applications," *e-Prime - Advances in Electrical Engineering, Electronics and Energy*, vol. 9, p. 100641, Sep. 2024, doi: 10.1016/j.prime.2024.100641.
- [35] A. Ahmad, D. Choi, and S. Ullah, "A compact two elements MIMO antenna for 5G communication," *Sci Rep*, vol. 12, no. 1, p. 3608, Dec. 2022, doi: 10.1038/s41598-022-07579-5.
- [36] S. Tariq, S. I. Naqvi, N. Hussain, and Y. Amin, "A Metasurface-Based MIMO Antenna for 5G Millimeter-Wave Applications," *IEEE Access*, vol. 9, pp. 51805–51817, 2021, doi: 10.1109/ACCESS.2021.3069185.
- [37] A. Sarkar, A. H. Naqvi, and S. Lim, "(40 to 65) GHz Higher Order Mode Microstrip-Based Dual Band Dual Beam Tunable Leaky-Wave Antenna for Millimeter Wave Applications," *IEEE Trans. Antennas Propagat.*, vol. 68, no. 11, pp. 7255–7265, Nov. 2020, doi: 10.1109/TAP.2020.2995430.
- [38] Q.-C. Ye, Y.-M. Zhang, J.-L. Li, G. F. Pedersen, and S. Zhang, "High-Isolation Dual-Polarized Leaky-Wave Antenna With Fixed Beam for Full-Duplex Millimeter-Wave Applications," *IEEE Trans. Antennas Propagat.*, vol. 69, no. 11, pp. 7202–7212, Nov. 2021, doi: 10.1109/TAP.2021.3109592.
- [39] Q. Xuan Lai, Z. L. Hu, and Y. M. Pan, "A Simple Decoupling Method for Wideband Millimeter-Wave MIMO Magnetoelectric Dipole Antenna Array Using Parasitic Stubs," *IEEE Trans. Antennas Propagat.*, vol. 72, no. 10, pp. 7470–7479, Oct. 2024, doi: 10.1109/TAP.2024.3443700.
- [40] F. Arshad, A. Ahmad, Y. Amin, M. A. B. Abbasi, and D. Choi, "MIMO antenna array with the capability of dual polarization reconfiguration for 5G mm-wave communication," *Sci Rep*, vol. 12, no. 1, p. 18298, Oct. 2022, doi: 10.1038/s41598-022-23163-3.
- [41] J. Khan, S. Ullah, U. Ali, F. A. Tahir, I. Peter, and L. Matekovits, "Design of a Millimeter-Wave MIMO Antenna Array for 5G Communication Terminals," *Sensors*, vol. 22, no. 7, p. 2768, Apr. 2022, doi: 10.3390/s22072768.
- [42] K. Raheel, A. W. Ahmad, S. Khan, S. A. A. Shah, I. A. Shah, and M. Dalarsson, "Design and Performance Evaluation of Orthogonally Polarized Corporate Feed MIMO Antenna Array for Next-Generation Communication System," *IEEE Access*, vol. 12, pp. 30382–30397, 2024, doi: 10.1109/ACCESS.2024.3369251.
- [43] D. A. Sehrai *et al.*, "A High Gain Array Based Millimeter Wave MIMO Antenna With Improved Isolation and Decorrelated Fields," *IEEE Access*, vol. 12, pp. 89794–89803, 2024, doi: 10.1109/ACCESS.2024.3418843.
- [44] S. Tariq, A. A. Rahim, W. T. Sethi, F. Faisal, and T. Djerfafi, "Highly isolated pin-loaded millimeter wave MIMO antenna array system for IoT-based smart environments," *AEU - International Journal of Electronics and Communications*, vol. 187, p. 155500, Dec. 2024, doi: 10.1016/j.aeue.2024.155500.
- [45] A. Sufyan *et al.*, "Self-Decoupled 8-Element Dual Polarized MIMO Antenna for B5G Handsets With Sub-6 GHz and mmWave Integration," *IEEE Access*, vol. 12, pp. 167324–167332, 2024, doi: 10.1109/ACCESS.2024.3491867.



PARVEEZ SHARIFF B. G. (Graduate Student Member, IEEE) received the B.E. degree in telecommunication engineering and the M.Tech. degree in digital electronics and communication systems from Visvesvaraya Technological University, Belagavi, India, in 2007 and 2009, respectively. He is currently pursuing the Ph.D. degree with the Electronics and Communication Engineering Department, Manipal Institute of Technology, Manipal, India. His research interests include microstrip antenna, array antenna, flexible antenna, MIMO antenna and metamaterial structure. He is a Life Member of ISTE, India.



TANWEER ALI (Senior Member, IEEE) is currently an Associate Professor with the Department of Electronics and Communication Engineering, Manipal Institute of Technology, Manipal Academy of Higher Education, Manipal. He is an Active Researcher in the field of microstrip antennas, wireless communication, and microwave imaging. He has published more than 130 papers in reputed web of science (SCI) and Scopus indexed journals and conferences. He has

led seven Indian patents, of which three have been published. He is on the board of reviewer of journals, such as IEEE TRANSACTIONS ON ANTENNAS AND PROPAGATION, IEEE ANTENNAS AND WIRELESS PROPAGATION LETTERS, IEEE ACCESS, and many other journals. He has been listed in top 2% scientists across the world for the year 2021 and 2022 by the prestigious list published by Stanford University, USA, indexed by Scopus.



PALLAVI R. MANE (Senior Member, IEEE) received the B.E. degree in electronics and communication engineering from the Gogte Institute of Technology, India, in 1996, the M.Tech. degree in digital electronics and advanced communication from the National Institute of Technology, Surathkal, Karnataka, India, in 2002, and the Ph.D. degree in electronics and communication engineering from Manipal Institute of Technology (MIT), MAHE, Manipal, for the

thesis in network coding, in 2014. She is currently a Professor with the Department of ECE, MIT, MAHE. She has authored several papers in international conferences and journal proceedings. Her research interests include network coding, source, and channel coding, and communication engineering.



SAMEENA PATHAN is currently an Assistant Professor with the Department of Information and Communication Technology, Manipal Institute of Technology, Manipal Academy of Higher Education, Manipal. Her research interests include pattern recognition, medical image analysis, artificial intelligence, and machine learning.



SAAD HASSAN KIANI completed his BS and MS degrees from the City University of Science and Information Technology and Iqra National University in 2014 and 2018, respectively. He obtained his Ph.D. degree from IIC University of Technology, Kingdom of Cambodia, in 2022. He was part of the Smart Systems Engineering Lab at the College of Engineering, Prince Sultan University, Kingdom of Saudi Arabia, from July 2022 to January 2023. He served as a Research

Scientist (remote) with the RF Microsense Research Group at Istanbul Medipol University, Istanbul, Turkey, and the Advanced Electromagnetics

Research Group at King Abdulaziz University, Jeddah, Kingdom of Saudi Arabia, from 2023 to 2024. Currently, he is serving as a Postdoctoral Researcher at Fakulti Teknologi dan Kejuruteraan Elektronik dan Komputer (FTKEK), Universiti Teknikal Malaysia Melaka (UTeM), Malaysia. His research interests include MIMO antenna systems, slot antennas, origami and kirigami antennas, multiband antennas, implantable antennas, frequency-selective surfaces, and metasurfaces.



BAL S. VIRDEE received the B.Sc. and MPhil degrees in Communications Engineering from the University of Leeds, UK, and his Ph.D. in Electronic Engineering from the University of London, UK. He has worked in industry for various companies including Philips (UK) as an R&D-engineer and Teledyne Defence and Space as a future products developer in RF/microwave communications. He has taught at several academic institutions before joining London

Metropolitan University where he is a Senior Professor of Communications Technology in the School of Computing and Digital Media where he is Head the Communications Technology Research Center. His research, in collaboration with industry and academia, is in wireless communications encompassing mobile-phones to satellite-technology. Prof. Virdee has chaired technical sessions at IEEE international conferences and published numerous research papers. He is Executive Member of IET's Technical and Professional Network Committee on RF/Microwave-Technology. He is a Fellow of IET and a Senior-Member of IEEE.

HALA MOSTAFA (Member, IEEE) received the Ph.D. degree in electrical engineering from the Faculty of Engineering and Applied Science, Memorial University, Canada, in 2014. From 2014 to 2015, she was a Research Scientist with Memorial University. She is currently an Assistant Professor with the Information Technology Department, College of Computer and Information Sciences, Princess Nourah bint Abdulrahman University, Riyadh, Saudi Arabia. Her main research interests include wireless communications, with a particular focus on smart antennas and wireless sensor networks.